Global and Planetary Change 216 (2022) 103921

Contents lists available at ScienceDirect

Global and Planetary Change

journal homepage: www.elsevier.com/locate/gloplacha

Rapid transformation of tundra ecosystems from ice-wedge degradation

M.T. Jorgenson [a,*], M.Z. Kanevskiy [b], J.C. Jorgenson [c], A. Liljedahl [d], Y. Shur [e], H. Epstein [f], K. Kent [f], C.G. Griffin [f], R. Daanen [g], M. Boldenow [h], K. Orndahl [i], C. Witharana [j], B.M. Jones [b]

[a] *Alaska Ecoscience, 2332 Cordes Dr., Fairbanks, AK, United States of America*
[b] *Inst. Northern Engineering, Univ. Alaska Fairbanks, United States of America*
[c] *U.S. Fish and Wildlife Service, Fairbanks, AK, United States of America*
[d] *Woods Hole Research Center, Falmouth, MA, United States of America*
[e] *Inst. Northern Engineering, Univ. Alaska Fairbanks, Fairbanks, AK, United States of America*
[f] *University of Virginia, Charlottesville, VA, United States of America*
[g] *Alaska Div. Geol. & Geophysical Surv., Fairbanks, AK, United States of America*
[h] *US Fish and Wildlife Service, Anchorage, Alaska, United States of America*
[i] *Northern Arizona University, United States of America*
[j] *University of Connecticut, Storrs, CT, United States of America*

ARTICLE INFO

Editor: Jed O Kaplan

Keywords:
Arctic
Permafrost
Ice wedges
Thermokarst
Hydrology
Soils
Vegetation
Landscape change

ABSTRACT

Ice wedges are a common form of massive ground ice that typically occupy 10–30% of the volume of upper permafrost in the Arctic and are particularly vulnerable to thawing from climate warming. In assessing the patterns and rates of ice-wedge degradation in northeastern Alaska, we found degradation was widespread and rapidly transforming the microtopography, hydrology, soils, ground ice, and vegetation of tundra ecosystems through a sequence of degradation and stabilization stages. Across an extensive mapping area (30 km^2), thermokarst troughs and pits with open water (degradation-advanced) covered 0.7% overall and 1.6% in the oldest terrain in 2018. Within an area (0.5 km^2) of concentrated thermokarst, undegraded and degraded ice wedges together covered 29% of the area, and all degradation stages combined increased from 2% in 1950 to 19% area in 2018. Initial degradation peaked at 9% in 2000 and initial stabilization was trending upward at 12% area in 2018, indicating slowing degradation and a transition to stabilization. Integration and reorganization of the drainage network as troughs expanded and connected reduced impounded surface water and helped slow degradation. Degradation created large changes in microtopography, trough widths, water depths, depth to wedge ice, pH, soil and ground ice characteristics, and thermal regimes among stages. Community composition completely shifted from dominance of deciduous and evergreen shrubs in tussock tundra in the undegraded stage to dominance of aquatic mosses and forbs in flooded depressions in degradation-advanced stage. Soil slumping along trough margins and rapid colonization by aquatic mosses halted the degradation, and aquatic sedges became dominant in the stabilization-initial stage. In stabilization-advanced, aquatic mosses persisted and the diversity of wet-adapted forbs, sedges, and mosses increased. Recovery back to tussock tundra, however, is unlikely. This decadal-scale transformation has major implications for arctic land cover, tundra productivity, lake expansion and drainage, soil-carbon balance, trace-gas emissions, and caribou and bird populations.

1. Introduction

Massive ground ice in the form of ice wedges is ubiquitous in the upper permafrost throughout the Arctic due to its very cold climate (Leffingwell, 1915; Black, 1952; Mackay, 1972; Romanovskii, 1985). Ice wedges are particularly sensitive to disturbance and climate warming because they form just below the seasonally thawed active layer (Brown and Grave, 1979; Kanevskiy et al., 2017). Degradation of ice wedges has

* Corresponding author.
E-mail addresses: ecoscience@alaska.net (M.T. Jorgenson), mkanevskiy@alaska.edu (M.Z. Kanevskiy), Janet_Jorgenson@fws.gov (J.C. Jorgenson), aliljedahl@whrc.org (A. Liljedahl), yshur@alaska.edu (Y. Shur), hee2b@virginia.edu (H. Epstein), kck7bw@virginia.edu (K. Kent), cg4pm@virginia.edu (C.G. Griffin), ronald.daanen@alaska.gov (R. Daanen), megan_boldenow@fws.gov (M. Boldenow), kmo265@nau.edu (K. Orndahl), chandi.witharana@uconn.edu (C. Witharana), bmjones3@alaska.edu (B.M. Jones).

https://doi.org/10.1016/j.gloplacha.2022.103921
Received 19 March 2022; Received in revised form 15 July 2022; Accepted 12 August 2022
Available online 23 August 2022

been observed throughout the Arctic, with the pace of degradation increasing rapidly during the last few decades (Jorgenson et al., 2006; Jorgenson et al., 2015a; Liljedahl et al., 2016; Steedman et al., 2016; Fraser et al., 2018; Farquharson et al., 2019). This degradation can radically transform arctic ecosystems (Martin et al., 2009; AMAP, 2017; Schuur and Mack, 2018), yet little is known how the degradation affects the hydrology, soils, vegetation, and wildlife.

Factors affecting ecological responses to climate change in the Arctic are being assessed on many fronts. Warming air temperatures have affected the water balance and surface hydrology of polygonal ground (Fortier et al., 2007; Liljedahl et al., 2012; Helbig et al., 2013). Permafrost degradation, resulting in a wide variety of thermokarst landforms, has increased dramatically (Kokelj and Jorgenson, 2013; Grosse et al., 2016). Vegetation is changing in response to temperature effects on nutrient cycling and competitive interactions among plant species (Blok et al., 2011; Heijmans et al., 2022), snow cover change (Sturm et al., 2005; Niittynen et al., 2020), and herbivory (Joly et al., 2009). While fire frequency has varied substantially in the past (Hu et al., 2015), recent large fires in the Arctic have led to rapid ice-wedge degradation (Jones et al., 2015; Chen et al., 2021) and changes in vegetation and soil organic carbon (Bret-Harte et al., 2013; Nitze et al., 2018; Heim et al., 2021). Forest and shrub migration into new areas, altitudinal increases in treeline, and shifts in dominance within plant communities have altered canopy and understory composition (Myers-Smith et al., 2011; Loranty and Goetz, 2012). Changes in fluvial regimes affect successional patterns and plant productivity (Raynolds et al., 2013; Liljedahl et al., 2020). Lake area has increased through shore erosion and decreased from drainage, with ice-wedge degradation usually an important factor (Nitze et al., 2017; Jones et al., 2022). Storm surges enhanced by sea-ice retreat have led to increased coastal erosion and salinization (Lantuit et al., 2013; Irrgang et al., 2022). Glacier melting has exposed new barren alpine areas subject to primary succession (Arendt et al., 2009) and affected the geomorphology of glacier-fed river systems (Moore et al., 2009). Increasing human populations and industrial activities also contribute to environmental changes, including ice-wedge degradation (Raynolds et al., 2014; Walker et al., 2022). Collectively, these drivers contribute to a diverse mosaic of early to late-successional ecosystems where change can occur abruptly through disturbance events (pulses) or gradually through successional processes or chronic stressors (Chapin et al., 2004; Jorgenson et al., 2015b). While the role of ground ice in general, and ice-wedge degradation in particular, is undoubtedly fundamental to many of these landscape changes, this uniquely arctic environmental factor remains inadequately understood.

Ice-wedge abundance is highly variable across arctic landscapes due to differences in surficial geology and terrain age (Kanevskiy et al., 2013; Couture and Pollard, 2017). Because ice wedges (see example in Fig. SI1) develop from annual contraction cracking and meltwater infilling (Leffingwell, 1915; Lachenbruch, 1962), the size of the wedges is closely related to landscape age and evolution (Jorgenson et al., 1998). The volume of wedge ice in the upper 3 m of permafrost typically ranges from 10 to 20% (Pollard and French, 1980; Kanevskiy et al., 2013; Couture and Pollard, 2017; Frappier and Lacelle, 2021), although newly exposed land may not yet have developed ice wedges, and old deposits may have volumes of 30 to 40%. Moreover, in extremely ice-rich eolian silt of Pleistocene age (yedoma) in northern Alaska, syngenetic ice wedges that formed concurrent with loess deposition occupied 30 to 70% of the volume of ~40-m-thick deposits (Kanevskiy et al., 2011). Quantifying ice-wedge volume is problematic, however, because surface patterns do not always reflect subsurface ice-wedges and there can be multiple generations of ice wedges of differing widths and depths (Black, 1976; Burn and O'Neill, 2015; Frappier and Lacelle, 2021). In addition to wedge ice, formation of segregated ice also contributes significant volumes of ground ice. For example, an ice-rich intermediate layer typically forms in the upper permafrost in response to ecological succession and active-layer adjustments, with pore and segregated ice frequently occupying 60–90% of the soil volume (Shur et al., 2005; French and Shur, 2010; Kanevskiy et al., 2013).

Ice wedges are highly vulnerable to both disturbance and climate warming, including summer off-road traffic (Brown and Grave, 1979), winter seismic exploration (Jorgenson et al., 2010a), gravel emplacement for roads and pads (Raynolds et al., 2014), road dust and impoundments (Walker et al., 2022), fire (Jones et al., 2015), shoreline erosion (Walker and Arnborg, 1963; Irrgang et al., 2022), and storm runoff (Fortier et al., 2007). Extremely warm and wet summers in 1989, 1998, 2004, and 2012 in northern Alaska are thought to have led to the onset of rapid ice-wedge degradation in that region (Jorgenson et al., 2015a), although there can be regional differences in timing (Frost et al., 2018). Once initiated, ice wedges typically go through a sequence of degradation and stabilization stages that are sensitive to both ground ice dynamics and ecological feedbacks (Jorgenson et al., 2015a). Previous episodes of degradation are evident in the presence of pool ice that filled the cavities of partially thawed ice wedges (Kanevskiy et al., 2017), deep thermokarst ponds, ice-wedge pseudomorphs, and other paleoenvironmental indicators (Harry and Gozdzik, 1988; Christiansen et al., 2016). When ice volume is sufficiently high, thermokarst lakes can form (Jones et al., 2022), and in places, such as in the Colville Delta, ice volumes are so high in abandoned floodplains deposits that most of the terrain has been converted to thermokarst lakes and drained-lake basins (Jorgenson et al., 1998).

To better understand the extent, nature, dynamics, and drivers of ice-wedge degradation, specific objectives of the study were to: (1) evaluate climate trends and identify extreme seasons affecting ice-wedge degradation; (2) document the extent and change rates of various stages of ice-wedge degradation and stabilization through remote sensing; (3) quantify ecological changes in microtopography, hydrology, permafrost soils, and vegetation in response to ice-wedge degradation; and (4) evaluate the climatic and biophysical drivers and feedbacks controlling degradation and stabilization of ice wedges. This study replicates the approach used by Jorgenson et al. (2015a, 2015b) to assess the response of ecosystems to ice-wedge degradation in wet/moist tundra near Prudhoe Bay, but differs in that this study investigated changes in tussock tundra in the Arctic National Wildlife Refuge in a region that provides critical calving habitat for the Porcupine caribou herd.

2. Regional setting

The study area is near the Jago River (Lat. 69.75, Long. -143.61) in northeastern Alaska (Fig. 1). Vegetation in the area is dominated by tussock sedge-dwarf shrub tundra, which is the fifth most abundant (520 km^2) vegetation type in the circumpolar Arctic (Raynolds et al., 2019). The surficial materials of Quaternary and Tertiary age (QTsg) are composed of silty sand, sand, and gravelly sand of fluvial or glaciofluvial origin (Carter et al., 1986). We reinterpreted the slightly pebbly, slightly saline, sandy diamicton previously mapped as QTsg to be a sandy glacial till, consistent with the occurrence of old buried glacial ice at Kaktovik (Kanevskiy et al., 2013). This deposit has abundant, well-developed ice wedges (Carter et al., 1986), and is representative of terrain with moderate to high ground ice content that is widely distributed across northern Alaska (Jorgenson et al., 2008; Kanevskiy et al., 2013) and the Arctic (Brown et al., 1997). Permafrost temperatures in the region have warmed 1.5–3 °C from 1985 to 2004 (Osterkamp and Jorgenson, 2006).

3. Materials and methods

3.1. Sampling design

This study compiled data from several projects that used remote sensing of a time-series of imagery from 1950 to 2019 and field sampling to assess ecosystems responses to ice-wedge degradation and stabilization from 2009 to 2018. The remote sensing included: (1) mapping waterbody types and geomorphic units over an extensive area (5 × 6 km) to assess distribution of thermokarst troughs and pits. Within a

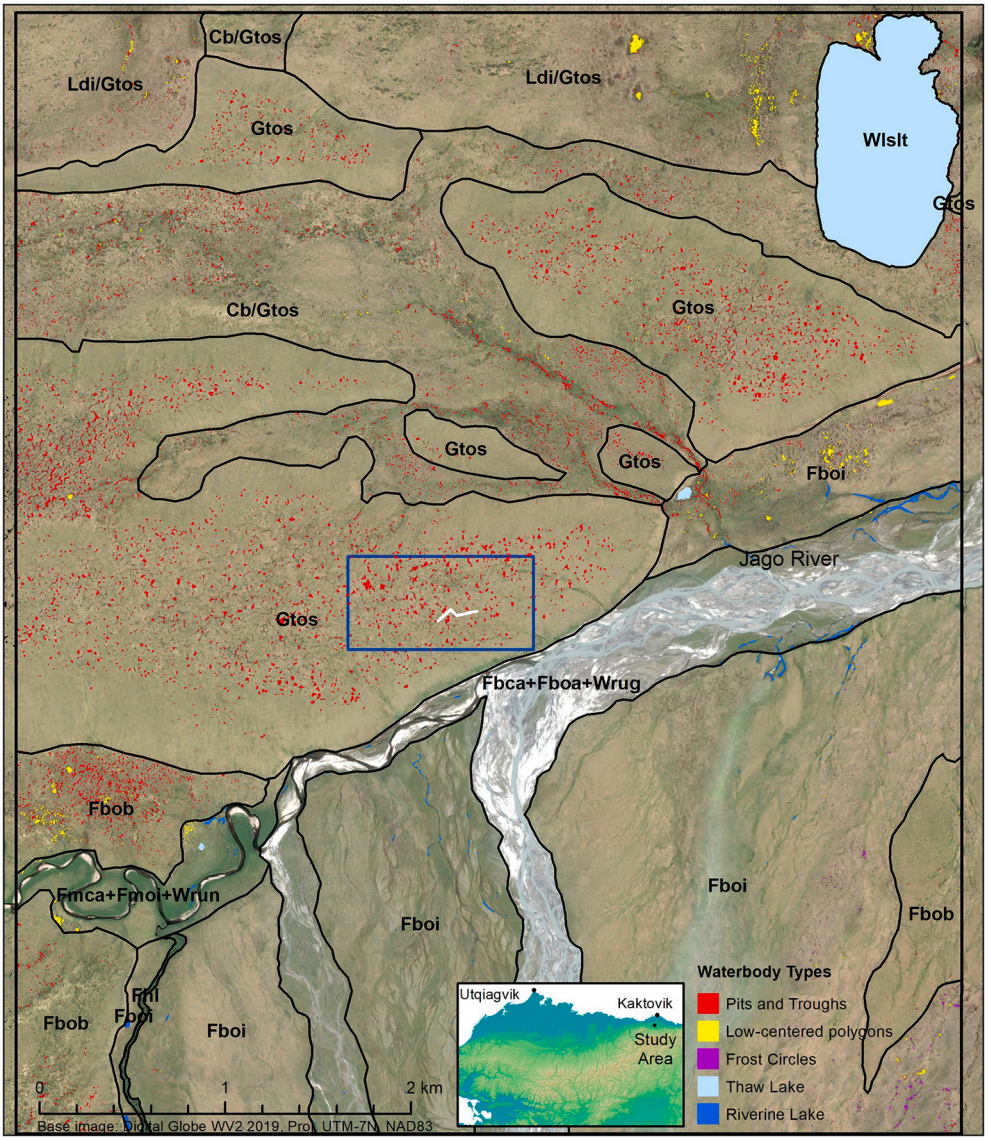

Fig. 1. Locations of the Jago study area in northern Alaska (inset), the intensive study area (blue box), monitoring transect (white line), and map of waterbody types (legend) in relation to geomorphic units (black) in the extensive study area. Geomorphic units include lowland headwater floodplain (Fhl), braided channel deposits-Active (Fbca), braided overbank dep.-inactive (Fboi), braided overbank dep.-abandoned (Fbob), meander overbank dep.-inactive (Fmoi), meander channel dep.-active (Fmca), drained-lake basin (Ldi), basin colluvium over till (Cb/Gtos), sandy till-old (Gtos), upper perennial river-glacial (Wrug), upper perennial river-non-glacial (Wrun), and shallow isolated thaw lake (Wlsit). (For interpretation of the references to color in this figure legend, the reader is referred to the web version of this article.)

smaller intensive study area (0.5 × 1 km) with abundant thermokarst features, remote sensing included: (2) grid sampling of changes in six stages of ice-wedge degradation using a time-series of historical imagery; (3) mapping changes in thermokarst troughs and pits; (4) mapping changes in drainage networks; and (5) mapping surface microtopography using a drone in 2018. For field monitoring of topography, water depths, and thaw depths over time (8/14/2009, 8/31/2011, 7/27/2016, 8/1/2018), we sampled every meter along a 250-m transect oriented to cross replicate patches with differing degradation stages (Fig. SI2). For monitoring hydrology, soil, and vegetation over time, we used stratified, targeted sampling to establish three replicate permanent plots in each degradation stage (total 18), with the replicates broadly distributed along or near the transect. Plots for the undegraded stage, however, were not established until 2018. A subset of monitoring plots had dataloggers for sampling soil temperatures. In addition, soil and/or vegetation were sampled in 57 temporary plots established within representative patches away from the transect to increase sample sizes for each stage.

Stratification by degradation/stabilization stages included polygon centers without ice wedges (PC), undegraded (UD), degradation-initial (DI), degradation-advanced (DA), stabilization-initial (SI), stabilization-advanced (SA) stages that were identified by previous studies (Jorgenson et al., 2015a; Kanevskiy et al., 2017); see Fig. SI3 for ground views of stages, and Fig. SI4 for airphoto characteristics. In 2018, we differentiated a seventh stage, stabilization-very advanced (SAV). We also differentiated secondary stages where permafrost coring revealed that degradation had been halted (H suffix, *i.e.*, DIH, DAH), or where the patches had become integrated into polygonal drainage networks (D suffix, *i.e.*, DID, DAD, SID). Most analyses focused on the primary stages, while permafrost analyses included the secondary stages.

3.2. Climate trends

Climate data were compiled from the National Climate Data Center (https://www.ncdc.noaa.gov/cdo-web/) for weather stations at Barter Island, Barrow, Kuparuk, and Deadhorse, and from the Alaska Ocean Observing System (https://portal.aoos.org/) for additional data for Barter Island. Climate data for Niguanak were obtained from the U.S. Geological Survey (https://www.sciencebase.gov/catalog/item/59d6a458e4b05fe04cc6b47e). Due to substantial data gaps for Barter Island, we correlated average daily temperatures with regional daily average temperatures for the other stations and used the mean difference to assign average daily temperatures (regional ave. + ave. difference of −1.0 °C) for missing data at Barter Island for summers (June-Aug.) that

had at least 80% observations. To extend the record for Niguanak, we calculated differences in mean summer air temperatures for Niguanak and Barter Island, then used the mean difference (2.2 °C) to estimate Niguanak temperatures back to 1947.

3.3. Remote sensing of thermokarst features

A time-series of high-resolution imagery was compiled for the extensive and intensive study areas. Airphotos were from 8/2/1950 (B&W, 0.5-m pixel resolution), 7/8/1978 (color-infrared, 0.9 m), 8/5/1988 (color-infrared, 0.1 m), and 9/9/2006 (color, 0.4 m). Satellite images were from 7/21/2000 (Ikonos, pan-sharpened, 1.0 m), 6/28/2014 (Geo-Eye 1, pan-sharpened, 0.4 m), and 7/12/2019 (WV2, pan-sharpened 0.5 m). An airphoto mosaic was produced from drone photography acquired on 7/31/2018 (color, 0.1 m). The imagery was geo-rectified to the 2018 ground-controlled airphoto mosaic.

Thermokarst waterbodies in the extensive area were mapped through spectral classification of the 2019 imagery and manually classified through image interpretation. Image classification was based on an unsupervised spectral classification (20 isoclasses) using the 4-band panchromatic-fused image from 2019. One class was interpreted to be associated with open water, while a second class was associated with aquatic sedge with abundant surface water. River water was not classified because of high spectral variability and confusion between turbid water and wet mud. A majority filter (4 pixel) was used to eliminate sparse occurrences and smooth boundaries before converting the raster classification to vector polygons. Polygons <2 m^2 were removed. The polygons were then manually classified to waterbody type, including water-filled thermokarst troughs and pits (TTP), low-centered polygons (PC, small waterbodies within polygon centers), frost circles (FC, water-filled frost scars common on saturated gravelly inactive floodplains), thaw lakes (TL, non-riverine), and riverine lakes (RLK, formed in high-water channels). Waterbody interpretation relied on waterbody shape and microtopographic context (Fig. SI5). Finally, waterbodies were assigned the geomorphic unit of the mapping polygon in which they occurred. Geomorphic units were mapped on-screen using ArcMap at 1:5000 scale based on manual image interpretation using the approach of Wells et al. (2020) and a landform-soil classification modified from Kreig and Reger (1982).

Thermokarst troughs and pits were mapped within the intensive area through photo-interpretation and on-screen digitizing using the image time-series. TTP were primarily associated with the DA stage, but also included portions of the SI stage with abundant standing water. The features (minimum 5 m^2) were mapped on-screen using ArcMap at 1:200 scale. Polygons were attributed with year and unique ID to track waterbodies over time.

Degradation stages were photo-interpretated and classified at 200 grid points (50-m spacing) for seven periods from 1950 to 2018. The primary stages were further subdivided depending on whether the points occurred in a connected drainage network (D suffix added). For 1988 and 2018 when imagery had very high resolution and spectral quality, six vegetation types also were photo-interpreted, including low shrub (LS), tussocks (TT), moist sedge-shrub (MS), wet sedge (WS), and open water (OW).

Polygonal drainage networks (water-tracks) were mapped by photo-interpreting flow patterns evident in 1988 and 2018 imagery. Flow patterns and connections were identified by the robust sedge growth in troughs (bright red on CIR, bright green on orthomosaics). In some instances, multiple troughs appeared connected but close inspection at higher resolution revealed higher elevation blockages that prevented connection to the network.

Microtopography and orthoimagery for the intensive area were derived from high-resolution airphotos (3-cm resolution) that were acquired by a drone (DJI Phantom 4) flown at 100-m altitude. To control the photogrammetry, 12 ground control points (GCP) were established using differential GPS corrections (±2 cm RMS) relative to a permanent benchmark (±2 cm RMS) differentially corrected to the CORS network (NAVD88, Geoid-12b). An orthophoto mosaic (10-cm resolution) and digital elevation model (DEM, 20-cm resolution) were produced using Pix4D software and the GCPs for geodetic control. The software reported an overall georeferencing error of 0.26 m RMS.

3.4. Fieldwork on ecological changes

Field data collection included transect-level data on microtopography and plot-level data on site environmental conditions, soil stratigraphy, soil physical properties, soil thermal regimes, and vegetation composition (Table SI1). Microtopography, water, and thaw depths were measured every 1 m along the permanent 250-m transect that was established in 2009. Ground- and water-surface elevations were measured with an autolevel relative to the benchmark (T1–092 BM). Thaw depths below ground surface were measured with a metal probe.

Site descriptions included information on observers, location, plot type, topography, geomorphology, soils, hydrology, and vegetation using the ecological land classification approach of Jorgenson et al. (2009). Photographs of vegetation and soil cores were taken each site. Data were reviewed after fieldwork for consistency and completeness, and data summarizing soil and vegetation characteristics were added to the site-level data.

Soil stratigraphy was described from 95 profiles (22 permafrost cores in 2009, 23 active-layer pits in 2011, 50 permafrost cores in 2018) at 58 sites (14 monitoring sites were repeated in 2018) and samples were taken from 60 cores for physical analyses. In unfrozen active-layer soils, we extracted 30-cm diameter soil plugs with a shovel for subsampling with knives or small corers. For frozen soils, we used a SIPRE corer (7.5 cm diam.) and cored to 1–5.2 m depths. Soil stratigraphy was described according to Natural Resources Conservation Service field sampling methods. Coarse-fragment (>2 mm) percentage was visually estimated. Cryostructures were described according to French and Shur (2010). Peat types were differentiated by dominant plant macrofossils identifiable in the field with a hand lens. Soil samples were obtained every ~20 cm with additional samples taken from thin, distinctive horizons. For most samples, sample dimensions were measured for volumetric analyses. In the field, determinations were made for wet weights, and soil pH and electrical conductivity were measured in thawed liquids or a saturated paste with a portable meter calibrated daily. In the lab, samples were dried at 60 °C for ~8 days and weighed for calculating bulk density, gravimetric and volumetric moisture contents, and excess-ice contents.

Soil temperatures were measured near the surface (−3 cm depth) at 14 plots (2 or 3 within 5 stages) and in the upper permafrost (−50 or −65 cm) at 6 sites. Ten sites had complete records for 2009–2013, 6 sites had records extending to 2018, and 4 sites had complete records for only 1–2 years. Temperatures were recorded every 2 h using a single- (Hobo U22) or two-channel (Hobo U23) datalogger.

Vegetation cover was sampled in 18 permanent monitoring plots during three periods and at 47 inventory plots only once. For monitoring, three replicate permanent plots were sampled within six degradation stages (PC, UD, DI, DA, SA, SA) over three time periods (2009, 2011, 2016) for a total of 48 plots, although UD plots were not established until 2018. Plots were established in uniform patches, varying from 0.5 × 5 m in undegraded troughs (UD), to 4 × 10 m in polygon centers (PC); see Fig. SI3 for examples. At each monitoring plot, percent cover of each species was determined by ocular estimate in 2009 and by point sampling during 2011–2018. For point sampling, we used a vertically oriented laser pointer to determine species occurrence at 100 points per plot and noted "hits" for the first occurrence of a species at each point. For points with no live plant, we recorded litter (dead plant parts) if present, or bare soil if litter was absent. Surface water was recorded when present above or below live plants. After point sampling, the plots were examined for additional species and a cover of 0.1% was assigned to species that were present but not recorded by the point-

sampling. The total number of hits of each species was summed to determine percent cover. Vascular taxa were identified to species level, when possible, while non-vascular plants were identified to species only for dominant taxa. Voucher specimens were collected for problematic species; vascular taxa were identified by the authors, while bryophyte and lichen specimens were identified by specialists. During data management, we tabulated the percent cover by site and year, assigned final taxonomic determinations for each species, and aggregated problematic (inconsistent identification) and trace species into higher taxonomic or growth form levels.

3.5. Data analysis

Data were managed within various frameworks. Remote sensing data of thermokarst features were maintained within ArcMap spatial geodatabases. The site, soil stratigraphy, soil physical properties, and vegetation data were maintained in an Access relational database. Transect monitoring data resided in Excel that allowed all data to be linked to benchmark elevation. Temperature data were maintained within Excel so temperature data were actively linked to the calibration offsets, which were derived from the spring and fall water phase changes (zero curtain).

Descriptive statistics were generated to compare differences among degradation stages. For site environmental factors, 95% confidence intervals were calculated to evaluate significance of differences among means. Vegetation monitoring data, which were collected within a more rigorous experimental design, were analyzed using a generalized linear model for fixed factors (repeated measures design) to evaluate differences in species composition among degradation stages. For each growth form, we tested for significance ($p < 0.05$) of effects of degradation stage and year. Pair-wise comparison among degradation stages and years were conducted using the Tukey-Kramer multiple comparison test. At the species level, we simply tabulated percent cover by degradation stage and year. Species composition differences among stages were analyzed for both the monitoring plots subset and all plots with nonmetric multidimensional scaling as a multivariate ordination technique using PC-ORD 6.0 (McCune and Grace, 2002). Ordination axis scores of plots were correlated with environmental data and presented as biplots, in which vector length and direction represent the strength and direction of the correlations.

4. Results

4.1. Climate trends

Mean summer (June-Aug.) air temperatures (MAST) at Niguanak (~20 km from the Jago study area) increased at a mean rate of 0.3 °C/decade from 1947 to 2021 based on measured and regionally correlated temperatures (Fig. 2, left, see Fig. SI5 for daily correlations). While regional correlations were only modestly strong ($R^2 = 0.60$), they were sufficient to identify the extremely warm summers in 1958, 1989, 1998, 2004, and 2012 (Fig. 2, middle). These extremely warm years (top 5%) were consistent with the climate records for Barrow (Fig. 2, right), Kuparuk, and Deadhorse (Fig. SI6, SI7), although 1958 at Niguanak was anomalous. Summer temperatures in 2018 during the last sampling period were unusually cold. When examining the longer and more complete record for Barrow, extremely warm-wet summers included 1930, 1989, 2004, 2013, 2017, and 2019, indicting a trend toward more frequent warm-wet summers. Note that 1998 and 2012 were warm but not wet. We used these unusually warm-wet summers to help interpret trends in ice-wedge degradation.

4.2. Remote sensing of thermokarst extent, patterns and rates

Analysis of the patterns and rates of landscape change were based on four different mapping approaches. Within the broader extensive area

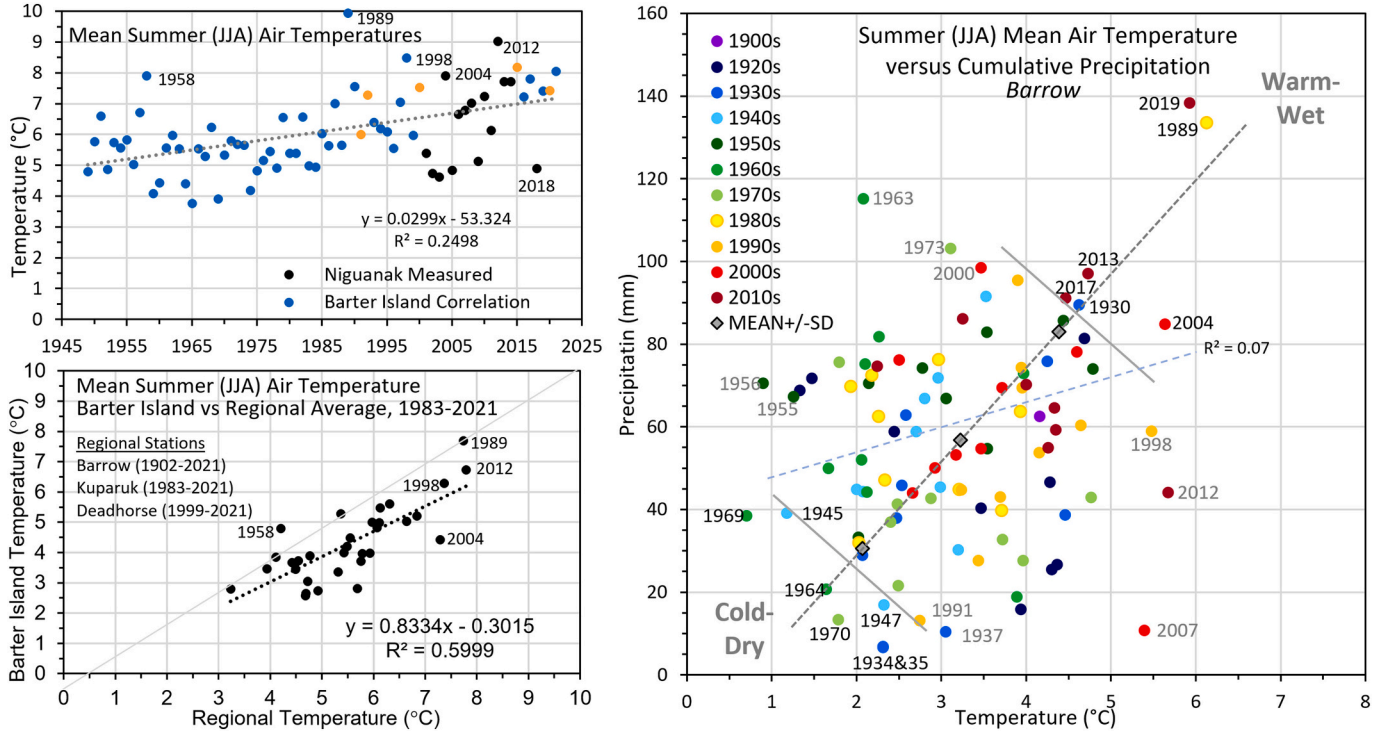

Fig. 2. Mean summer (June-Aug.) air temperatures (MSAT) measured and estimated for the nearby climate station at Niguanak (upper left), correlation of MSAT at Barter Island to the regional average (lower left), and plot of MSAT *versus* cumulative summer precipitation for Barrow (right). In the right plot, the gray dashed line is the axis for the trend from cold-dry to warm-wet based on the mean ± SD of the temperature and precipitation values, with the perpendicular bars differentiating the extreme 5% years along that axis. Regression line (blue dashed) indicates little relationship ($R^2 = 0.07$) between precipitation and air temperature. (For interpretation of the references to color in this figure legend, the reader is referred to the web version of this article.)

(30 km^2), waterbodies were mapped through image processing to assess the distribution of thermokarst troughs and pits (TTP). Within a small intensive area (0.5 km^2), TTPs were manually mapped to quantify rates of change, degradation stages were photo-interpretated across a systematic grid to assess changes by stage, and polygonal drainages were mapped to quantify network changes. These are described below.

Waterbody mapping and classification in the extensive study area revealed large differences in small waterbody types (excluding rivers and large lakes) among geomorphic units in 2019 (Figs. 1 and 3). Overall, areal extent of waterbodies associated with TTPs (0.7% area) was seven-fold higher than in low-centered polygons (LCP, 0.1% area), while extent of flooded frost circles was negligible (0.002%). Similarly, density of TTP (272/km^2) was ten-fold higher than LCP (23/km^2). Mean size of TTP (25.3 m^2) was two-thirds the size of LCP (39.7 m^2). When comparing geomorphic units, TTP extent was highest on old sandy till (1.6%) and abandoned braided overbank deposits (1.1%), and lowest on active and inactive floodplain deposits (0–0.3%). TTP densities were an order of magnitude higher on old sandy till (464/km^2), abandoned braided overbank deposits (564/km^2), and basin colluvium over till (567/km^2) compared to active (1/km^2) and inactive floodplain deposits (23/km^2). Mean size was highest in old sandy till (35.3 m^2) and lowest in active braided channel deposits (8.7 m^2).

Manual photo-interpretation and mapping of TTP within the intensive study area using the time-series of geo-rectified imagery showed large increases in total area, density, and mean size (Fig. 4, Fig. SI8). Percent area increased consistently from 1955 to 2000, increased abruptly from 2000 to 2006, and then decreased slightly. TTP density increased most rapidly from 1955 to 1978, a bit more slowly until 2006, and then decreased slightly. Mean size showed little change until 2000 and then increased abruptly until 2006. Together, they show that the early 2000s was a period of rapid thermokarst expansion with little change after 2006.

Photo-interpreted grid-sampling of five primary degradation stages across seven high-resolution images from 1950 to 2018 found a 58% decrease in areal extent of undegraded ice wedges from 26.0% in 1950 to 10.0% in 2018, with a noticeable acceleration between 1988 and 2000 and slowing after 2000 (Fig. 5 left, Fig. SI9). The areal extent of the degradation-initial (DI) peaked at 9.0% in 2000 and rapidly dropped to 1.0% by 2018, with most of this stage transitioning to stabilization-initial (SI), which reached 12.5% by 2018. Degradation-advanced (DA) gradually increased until 2000, then abruptly increased and peaked at 4.5% during 2006–2014 before slightly declining. Stabilization-advanced (SA) was absent until 2000, and gradually increased to 2.0% by 2018, as a small portion of SI transitioned into SA. With all stages combined, the area of degraded ice wedges increased nearly ten-fold from 2% in 1950 to 19% in 2018. When the areas of undegraded and degraded wedges were combined, the grid sampling estimated ice wedges underlay 29% of the surface, with the relative percent area of degraded wedges increasing from 7% in 1950 to 66% in 2018.

Percent volume of ice wedges was estimated to be 24.9% in the top 1 m and 14.5% in the top 3.5 m of permafrost, based on an initial surficial coverage of 29%, an average width of 4.5 m at the top of the wedge, and a wedge depth of 3.5 m. The overall extent of ice wedges, however, probably is underestimated (roughly 5–10%) because ice wedges often underly polygonal rims that were grouped with PC and we frequently encountered ice wedges in PC while coring. Note that the degradation of ice wedges typically is limited to the top 0.5–0.8 m, with the deeper portion of the wedges unaffected.

The grid points also were characterized as to whether they were isolated from or connected to the drainage network (connected troughs), there was an abrupt shift toward drainage integration with the secondary drainage-integrated SI class (SID) increasing from 2% in 1988 to 8% in 2018 (Fig. 5 right). The drainage integration of the DI stage (DID) peaked in 2000, with most of this stage transitioning into the SID stage.

Vegetation changes from 1988 to 2018, evident from the photo-interpreted grid sampling, were closely linked to the degradation/stabilization. Moist sedge-dwarf shrub decreased from 47.5% to 41.5% area (−6% absolute change) and tussock tundra from 36% to 33.5% (−2.5%). Increases were observed for aquatic sedge from 5% to 9.5% (4.5%), wet sedge from 5% to 8% (3%), and open water from 2% to 3% (1%). No change was observed for low shrub (4.5% of area). In terms of relative percent, tussock tundra and moist sedge-dwarf shrub combined decreased by 19.5%.

When comparing the TTP areal extent among remote sensing techniques within the common intensive study area (see Fig. SI10), TTP coverage was 3.9% in 2019 for the image processing technique (emphasizing DA stage with open water) *versus* 3.5% for DA in 2018 from the grid-point sampling. The manual delineation of TTP was 10.6% in 2018, intermediate between 3.5% for DA and 16% for DA and SI combined from the grid-point sampling. The similarity between the image processing and grid-point sampling indicates open water in the DA stage was consistently differentiated, but the substantially higher coverage of TTP by manual delineation indicates the more water-flooded and less vegetated conditions of SI were included. SI can have a wide range of characteristics from mostly water with low sedge cover to nearly complete robust sedge cover with shallow water underneath. The TTP extent mapped through image processing (3.9%, primarily DA), however, is only a small fraction of the total thermokarst-affected areas (19%, DI through SA stages) determined by grid-point sampling, with 100% of the automated polygons within the manually delineated polygons.

The polygonal drainage networks (water-tracks) in 1988 and 2018 within the intensive study area mapped using the highest quality images

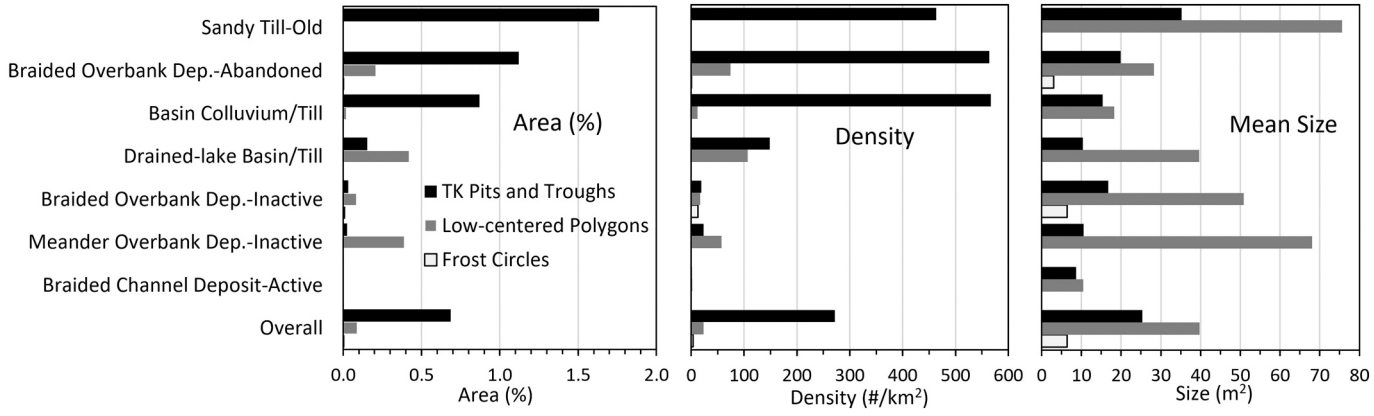

Fig. 3. Area (%), density (#/km^2), and mean size (m^2) of waterbody types by geomorphic units within the extensive study area at Jago, northern Alaska. Riverine waterbodies and the large thaw lake (Wlsit) shown on Fig. 1 are not included.

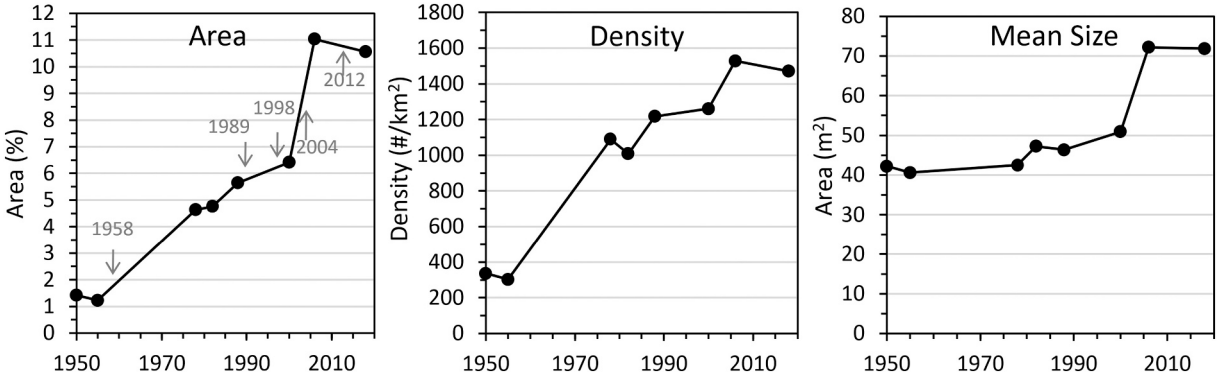

Fig. 4. Area (%), density (#/km^2), and mean size (m^2) of thermokarst troughs and pits within the Jago intensive study area, northern Alaska. Arrows identify years with extremely warm-wet summers.

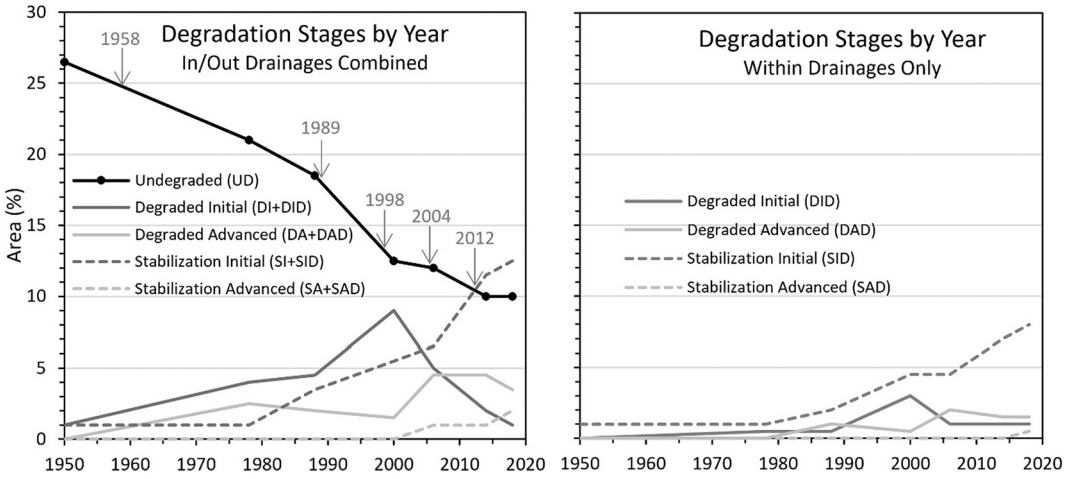

Fig. 5. Changes in percent area covered by degradation and stabilization stages over time (overall, left) and within drainages (connected troughs, right) based on photo interpretation at 200 grid points on a time series of airphotos and satellite images within the Jago intensive study area, northern Alaska. Arrows identify years with extremely warm-wet summers.

showed both increased integration of drainage connections and reorganization of the drainage network (Fig. 6). The total length of mapped drainages nearly doubled from 5.4 km in 1988 to 9.6 km in 2018 within the 0.5 km^2 study area. Primary drainages increased 15% from 3.5 km to 4.1 km, while secondary drainages increased 194% from 1.9 km to 5.4 km. The networks showed remarkable reorganization, with all primary channels shifting. Most notable was the capture of the upper portion of drainage D by E.

4.3. Microtopography and hydrology

Topographic surveys of the ground and water surfaces, and the permafrost table derived from late-July thaw-depth measurements (not yet maximum thaw), from 2009 to 2018 showed permafrost degradation has created large microtopographic relief and deep-water impoundments (Fig. 7). The DEM encompassing the monitoring transect showed a maximum difference in surface elevation of 2.2 m between a thermokarst pit and adjacent polygon centers, and an overall easterly gently sloping surface. The transect surveys found a maximum relief difference of 1.6 m between pit bottom and adjacent polygon centers. Within the polygon centers, microrelief typically varied by 0.2 m due to tussock and hummock microtopography. Over time, overall mean surface elevations along the transect decreased slightly from 152.89 m in 2009 to 152.85 in 2018, primarily due to the collapsing banks adjacent to expanding thermokarst pits, where lateral expansion of up to 2 m and surface collapse of up to 0.72 m were observed. In a few locations (especially 140–160 m distance), surface elevations within polygon centers varied by 0.2 m among years, depending on whether a tussock was encountered during surveying. Mean elevation of the permafrost table also showed a small decrease from 152.51 m in 2011 (first year of complete measurements) to 152.48 m in 2018, but this difference is small relative to annual and spatial variability. But there was substantially variability, with some areas showing minimum elevations in 2018 (at 65–100 m distance), while other sections showing an increase over time (at 150–160 m) due to sedge growth and peat accumulation. Within the DA stage, one pit (at 130 m) showed a lowering of the permafrost table resulting from continued thawing and degradation, although there was some variability from margins to center. In contrast, three pits (40, 105, and 230 m) showed raising of the permafrost table accompanied by a thickening permafrost layer above the ice wedges, indicating degradation had halted.

Water-surface elevations varied by an average of 0.14 m across 15 plots over the four survey periods, with a maximum annual range of 0.31 m in the active layer for tussock tundra. The consistent trend in water-surface elevations along the transect from 153.4 m (at 10 m) to 151.8 (at 236 m) indicate that the troughs were connected allowing water flow.

Environmental characteristics varied widely among stages (Fig. 8). Mean trough depth varied from 13 cm in UD to 64 cm in DA, and decreased to 7 cm in SAV, indicates that only the top 0.5–0.8 m of the ice wedges thawed and that substantial heave has occurred in the frozen soils in SAV. Mean trough width increased from 1.7 m in UD to 8.5 m in

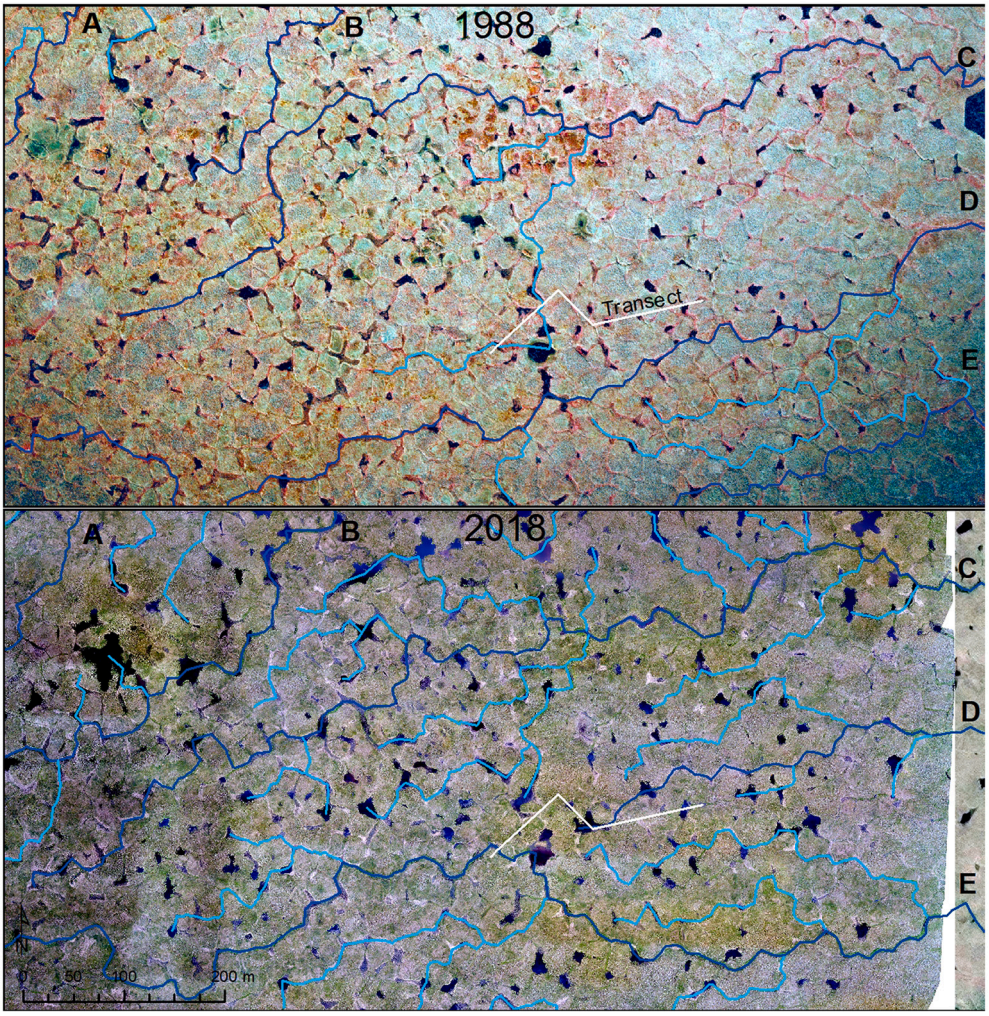

Fig. 6. Integration and reorganization of polygonal drainage networks from 1988 to 2018 resulting from thermokarst trough and pit development that created new surface topography and hydrologic connections. Letters denote major outlets and colors differentiate primary (dark blue) and secondary (light blue) drainages. (For interpretation of the references to color in this figure legend, the reader is referred to the web version of this article.)

DA, then decreased to 4.5–4.8 m in SI, SA, and SAV. The unusually wide depressions in DA, however, are inconsistent with the narrower troughs in the older stages, suggesting that recent trough expansion in the DA stage may be more intense than degradation in previous decades related to recent accelerated climate warming. Mean depth to ice-wedges increased slightly from 51 cm in UD to 65 cm in SA, with much larger depths in SAV (93 cm). Mean water depths increased from −19 cm (soil water below surface) in UD to +48 cm in DA and then decreased to −17 cm in SAV. Site pH (soil or water) increased from 6.0 in UD to 6.9 in DA, presumably due to water contact with thawed mineral soil and soil mixing during slumping, then decreased to 6.3 in SAV. Mean thickness of the soil surface organic layer (excluding cryoturbated, buried organics) ranged from 23 cm in UD to 31 cm in SI, but 95% confidence intervals mostly overlapped. Mean annual surface temperatures (−3 cm depth) during 2010–2013 was −4.4 °C in DI, increased to −1.3 °C in DA, and then decreased to −3.8 °C in SA (see Fig. SI11 for mean daily temperatures charts). Overall, these differences show tight linkages between environmental properties and degradation/stabilization stages.

Mean thermokarst ages, or years since initiation, based on imagery where sampling points with thermokarst patches were first observed after 1950, were similar for DI, DA, SI, and WT, ranging from 32 to 40 yrs. This age range was relatively narrow because 83% of the points where degradation was first observed occurred on the 1978–2000 images. The mean age for SA was 54 yrs., although 4 of 19 points were already SA in 1950.

4.4. Soils

Soil texture, surficial peat materials, cryostructures in frozen soil, and active/permafrost layers showed large transitions among stages (Fig. 9). Mean total soil thickness above the wedge ice varied slightly (55–66 cm) among most stages, except soils were unusually thick for the SAV stage (93 cm). Soil textures, aggregated into broad texture classes, were predominantly peat, loam/organic (mixed from cryoturbation), and loam (mostly slightly pebbly very fine sandy loam). Examples of soil profiles and cryostratigraphy are shown in Fig. SI12 and S13.

Identifiable peat materials, mostly from the surface fibric organic horizon (Oi), showed large changes through the degradation sequence. UD was dominated by feathermoss (*Hylocomnium splendens, Tomentypnum nitens*) and moss-woody material due to the prevalence of woody shrubs. While these materials persisted in lower amounts in DI, graminoid-woody peat became more evident. In DA, dead tussocks (*Eriophorum vaginatum*) predominated, with the small addition of fen mosses (*Hamatocaulis lapponicus, Calliergon giganteum*). During the SI stage, fen mosses and graminoid-fen moss showed large gains. In the SA stage, the graminoid-fen mosses persisted, and graminoid-woody increased substantially. By the SAV stage, feathermoss and moss-woody peat became reestablished to levels similar to UD. In

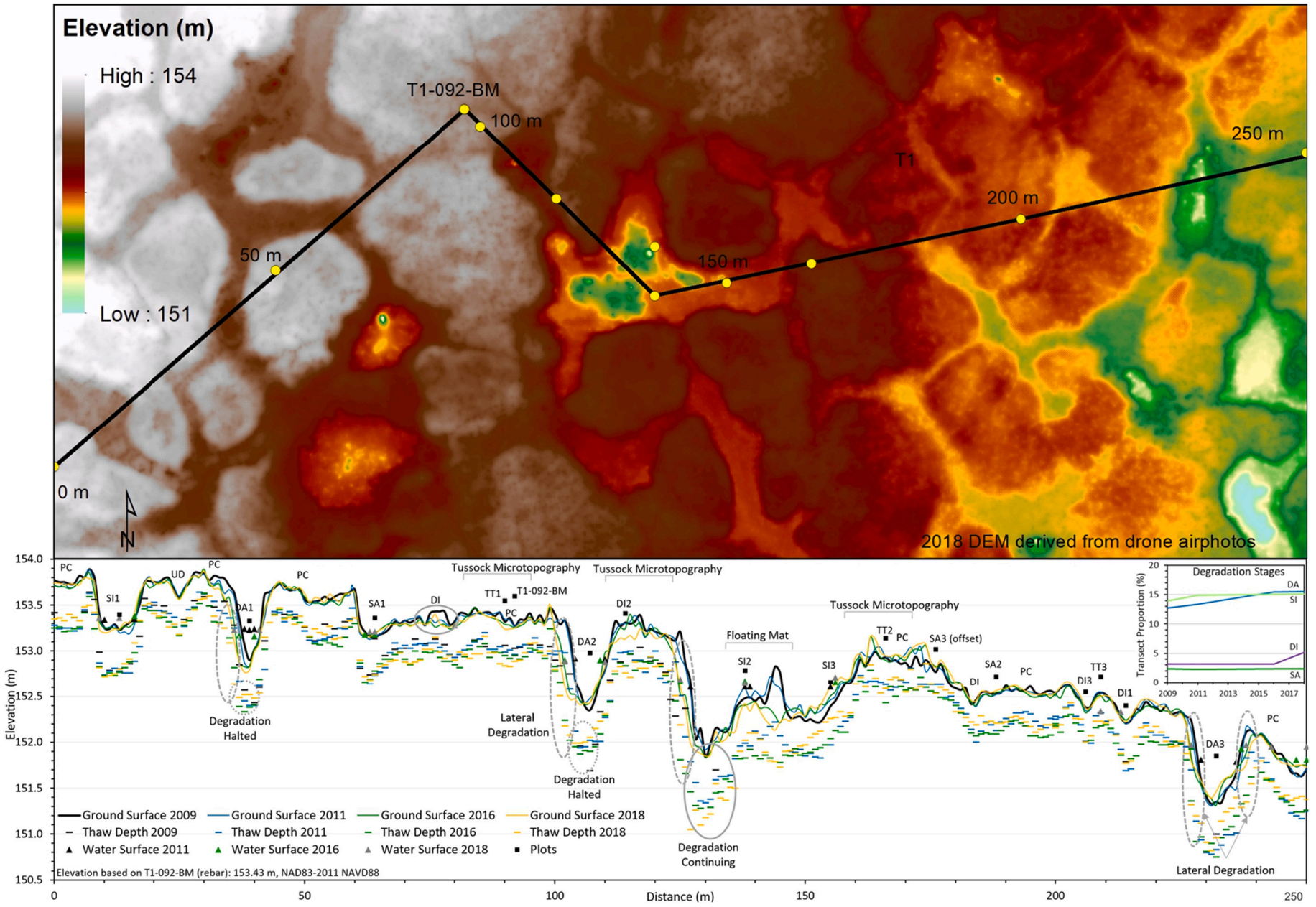

Fig. 7. A 2018 digital elevation model (DEM), and a topographic cross-section along black line on DEM showing elevations of the ground surface, water surface, and thaw depth in late July in 2009, 2011, 2016, and 2018 (bottom). Monitoring plots associated with five degradation stages are shown as black squares. Inset (upper right) in cross-section show changes in proportions of degradation stages from 2009 to 2018.

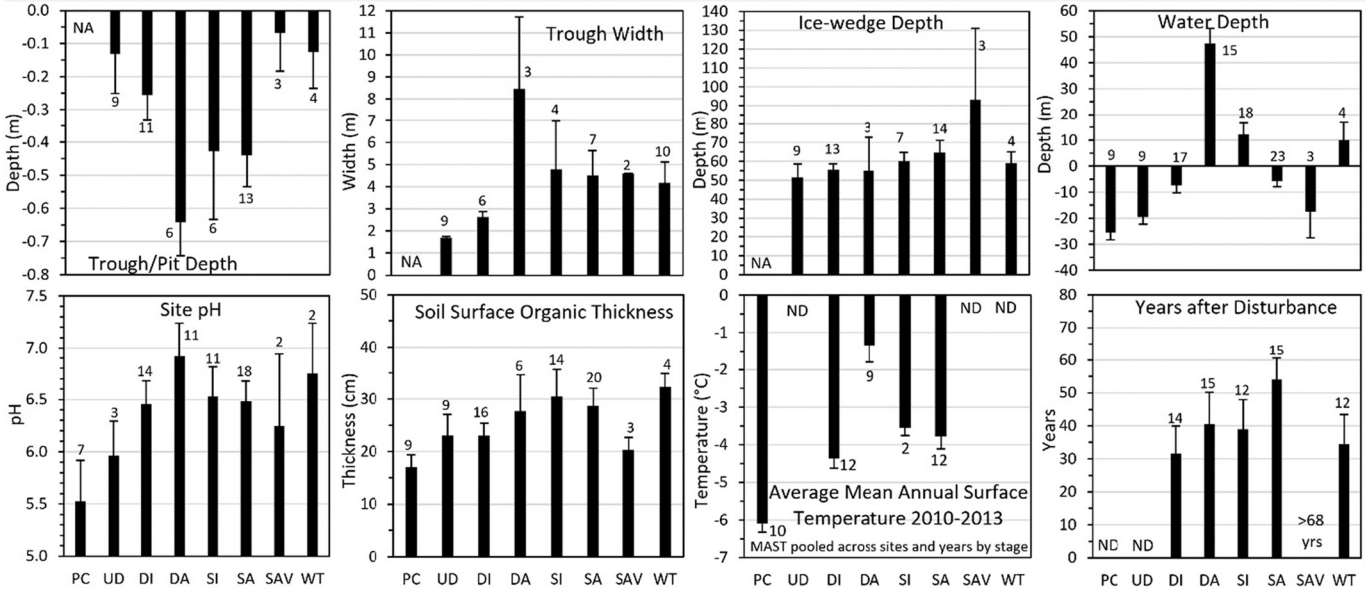

Fig. 8. Mean (±95% Confidence Interval) trough/pit depth, trough width, depth to ice wedge, water depth (negative when below surface), site pH, soil surface organic thickness, average mean annual soil surface temperatures, and years after disturbance for six degradation/stabilization stages at the Jago study area. Polygon centers and water tracks included for comparison. Sample sizes are above bars. Stages: PC-polygon centers, UD-undegraded, DI-degradation-initial, DA-degradation-advanced, SI-stabilization-initial, SA-stabilization-advanced, SAV-stabilization-very advanced, WT-water tracks.

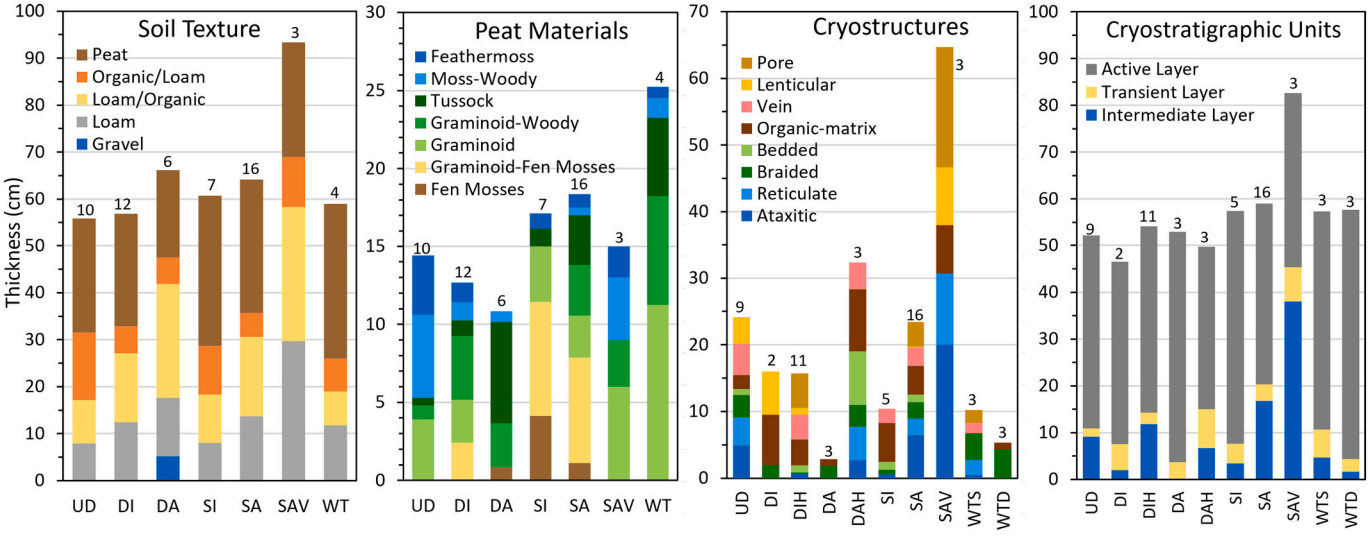

Fig. 9. Mean thickness of layers (all years combined) for soil texture, peat materials, cryostructures of frozen soils, and cryostratigraphic units by degradation-stabilization stage based on permafrost coring. Stages are UD-undegraded, DI-degradation-initial, DIH-degradation-initial-halted, DA-degradation-advanced, DAH-degradation-advanced-halted, SI-stabilization-initial, SA-stabilization-advanced, SAV-stabilization-very advanced, WTS-water-track-stabilizing, WTD-water-track-degrading. For soil and peat materials, water-tracks were combined, and the halted (H) stage was not differentiated. Sample sizes given above bars. Note position of layer in bars does not denote vertical sequence in profiles as positions and abundance vary among profiles.

comparison, water-tracks (DID and SID combined) had unusually thick graminoid and graminoid-woody peat, along with persistent dead tussock peat.

Total frozen soil above partially degraded ice wedges ranged in mean thickness from 2.8 cm in the DA stage to 64.7 cm in SAV, with large transitions in cryostructures among stages. The largest differences were for reticulate and ataxitic cryostructures, which were abundant in UD, absent in DI and DA, and redeveloped in SA and SAV. In SAV, reticulate and ataxitic cryostructures comprise nearly half the thickness of the newly aggraded permafrost above the wedge ice. These ice-rich layers contributed substantially to the heave of the surface over time. Also notable were the unusual thicknesses of ice-rich layers in the DAH stage, which may represent the initial stabilization of degrading ice-wedges, although this large accumulation of ground ice (especially bedded ice) was not evident in later stages.

Cryostratigraphic units, as interpreted from the sequence of cryostructures, were aggregated into three main layers with large differences among stages. Mean active-layer thickness (including frozen part) across all years ranged from 34.7 in DAH to 53.0 cm in WTD (SID and DID combined). Mean thickness of the transient layer, the portion of the upper permafrost that occasionally thaws over several years to decades, ranged from 1.8 in UD to 8.3 cm in DAH. Of 72 cores sampled (including PC sites), only 35 had evident transient layers, in part because differentiating the base of the frozen active layer from the transient layer

during late July sampling was not always clear. The intermediate layer, mainly differentiated by the occurrence of ataxitic, reticulate, braided, and bedded cryostructures, had the largest range in mean thickness from 0.0 cm in DA to 38.0 cm in SAV. When comparing years, 13 boreholes drilled above ice wedges in 2009 (3 DI, 3 DA, 3 SI, and 4 SA) were redrilled in 2018. Generally, the transient and intermediate layers were thicker above ice wedges at most sites by 2018 (except several DI and SA sites). In DA, mean thickness of the intermediate layer was 0 cm in 2009 compared to 15 cm (max. 31 cm) in 2018, although we note sampling was done about two weeks later in 2009, and 2018 was an unusually cold summer (Fig. 2). Evaluation of excess-ice content (EIC) revealed large differences between various soil layers. Mean EIC was 1.4% in the frozen part of the active layer ($n = 2$), 9.7% in the transient layer ($n = 6$), and 27.4% ($n = 26$) in the intermediate layer.

4.5. Vegetation

Vegetation structure and composition were completely transformed over the degradation sequence. Testing for the effects of degradation stage and year using a general linear model (repeated-measures design) found mean cover was significantly ($p < 0.05$) different among degradation stages for each growth form (aquatic mosses, other mosses, lichens, sedges, grasses, tussocks, and deciduous shrubs) except forbs and evergreen shrubs, and differed significantly among years only for sedges, with significant interactions between stage and year occurring only for sedges. When comparing stages, mean cover of deciduous shrub (years combined) was high in PC (24.9%), UD (18.3%), and DI (17.4%), and < 1% in DA, SI, and SA (Fig. 10, SI14). Evergreen shrub cover was highest in PC (18.5%), intermediate in UD (7.0%) and DI (2.9%), and absent in DA, SI, and SA. Forb cover highest in DA (12.8%). Grass mean cover was highest in DI (2.6%) and < 1.0% in all other stages. Tussock cover was high in PC (18.9%), persisted in DI (4.6%) with many dead tussocks, and was absent in DA, SI, and SA. Sedge cover was low in PC (9.7%), increased substantially from UD (24.0%) to DI (50.5%), dropped precipitously in DA (4.9%), and rebounded in SI (38.1%) and SA (41.8%). Lichen cover was highest in PC (4.5%), intermediate in UD (2.3%) and DI (1.1%), and absent in DA, SI, and SA. Aquatic mosses (brown fen mosses) were absent in PC (0.0%), at low levels in UD (2.7%) and DI (2.4%), and highest in DA (40.0%), SI (31.7%) and SA (69.7%). Cover of other moss (primarily feathermosses) was highest in PC (58.4%) and UD (77.1%), intermediate in DI (30.5%), absent in DA, and showed slight recovery in SI (5.1%) and SA (5.8%).

When considering temporal changes, the most notable changes over the seven years were: (1) a significant increase in sedges overall, with large and consistent increases in DI and SI, presumably in response to colonization and to changes in nutrient availability; and (2) a large increase in aquatic forbs and mosses in DA, with a smaller increase in sedges, due to rapid colonization of the newly developing thermokarst ponds. Small increases in sedge cover were also observed in PC and SA, however, and may simply be due to annual fluctuations with longer term sampling needed to confirm trends (Fig. SI15).

To evaluate compositional changes, non-metric multidimensional scaling (NMDS) of all plots across eight stages showed wide separation among stages, although some plots overlapped among stages indicating the transitional nature of species composition among stages (Fig. 11). The strongest environmental factors (length of vectors) associated with the variation in species composition were water depth and disturbance interval (age since disturbance). Soil thaw depth, water depth, pH, and disturbance interval were strong factors differentiating DA and SI from PC UD, and DI, while a thicker soil surface organic layer was strongly associated with SI and SA.

The subset of monitoring plots also showed a similar wide separation among the reduced set of stages in the NMDS. For these plots, there was little overlap in species space due to the more careful targeting of sites representative of each class. When evaluating correlations among growth forms included as a secondary matrix, evergreen and deciduous shrubs, tussocks, non-aquatic mosses, and lichens were strongly associated with PC (centers) and UD (troughs), whereas, aquatic mosses were strongly associated with DA, SI, and SA, while sedges were strongly associated with the gradient from DA to SA. Vectors tracking compositional shifts over time (gray lines) showed little directional change for most plots over 7 yrs., while two early succession plots (DA1 and DI1) showed a small consistent shift in species composition.

The mean cover of each species in the monitoring plots by stage and year is presented in Table 1. To briefly summarize, PC and UD were dominated by *Betula nana, Salix pulchra, Vaccinium vitis-idaea, Dryas integrifolia, Eriophorum vaginatum, Hylocomnium splendens*, and *Tomentypnum nitens*. In the transition to DI, 11 species were lost and 11 species gained, primarily due to the loss of evergreen shrubs and lichens and the gain of hydrophytic sedges *Eriophorum angustifolium* and *Carex aquatilis* and aquatic mosses. By the flooded DA stage, there was a nearly total transformation of species composition, with only *Eriophorum angustifolium* and *Salix pulchra* found in both UD and DA (along margins). DA was dominated by the aquatic moss *Hamatocaulis lapponicus* and the aquatic forb *Sparganium hyperboreum*, which did not occur in any other stage. SI was similar to DA, but with 6 species added (*e.g.*, *Eriophorum russeolum*), 1 species lost (*S. hyperboreum*), and an increasing dominance of sedges and the aquatic moss *Calliergon giganteum*. SA in comparison with SI gained 14 species (mostly mosses and forbs) and lost 2, with the aquatic mosses persisting or gaining in cover and the colonization of the sedge *Carex chordorrhiza*, a sedge unique to thick organic fen soils. Uncommon species ($n = 27$) were not included in the table. Mean cover by stage for

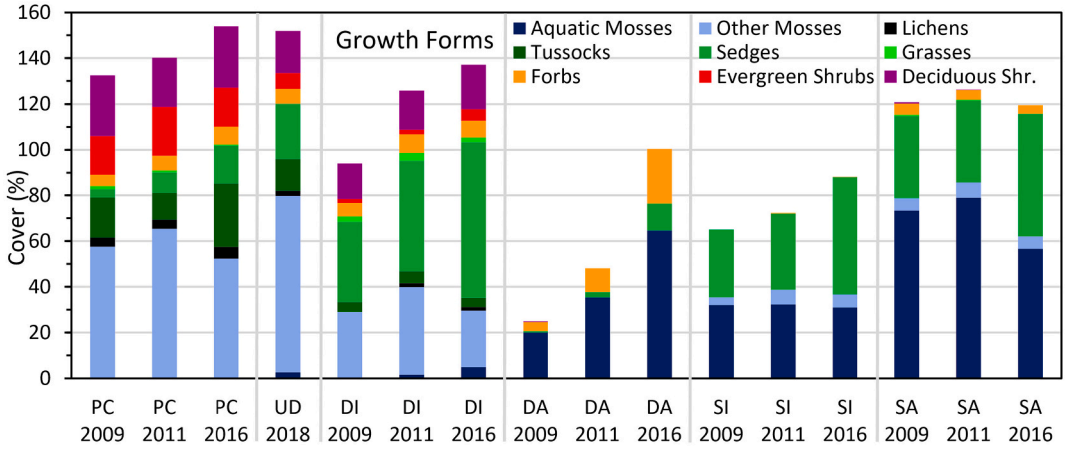

Fig. 10. Mean ($n = 3$) cover of plant growth forms by degradation/stabilization stage and year. Stages are PC-polygon center, UD-undegraded wedges, DI-degradation initial, DA-degradation advanced, SI-stabilization initial, SA-stabilization advanced.

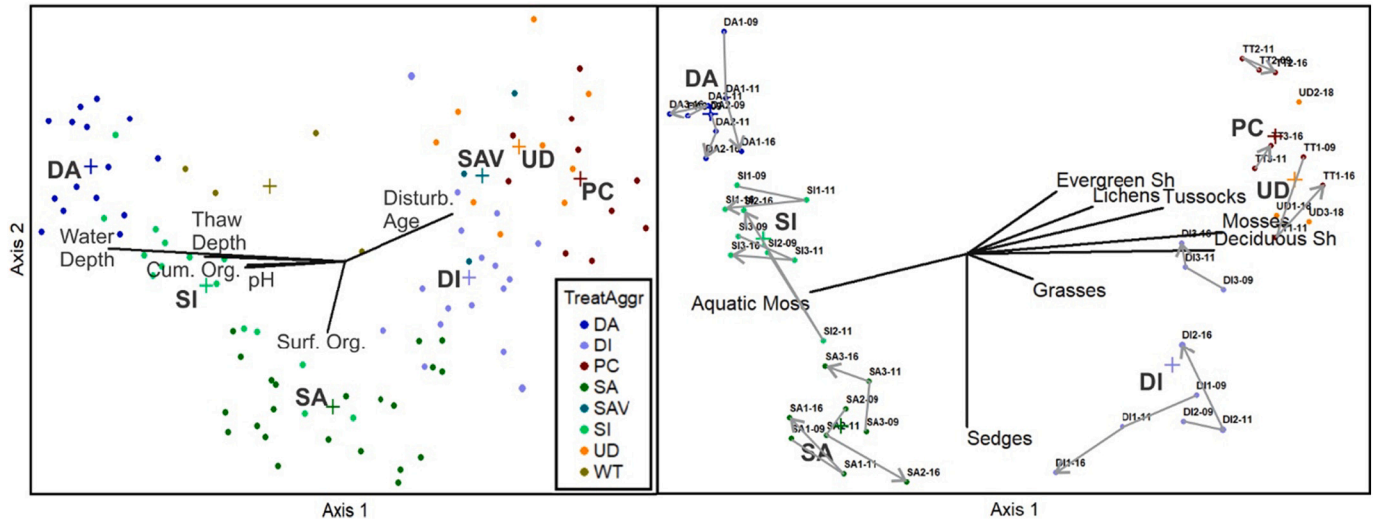

Fig. 11. Non-metric multidimensional scaling of vegetation composition of all plots (left, $n = 95$) and permanent monitoring plots (right, $n = 18$, repeated 2009, 2011, 2016, UD in 2018). Colors indicate degradation/stabilization stage. Vectors (black) indicate strength of correlation with environmental variables (left) and with growth forms (right). The crosses show centroid of each stage. For monitoring plots, gray vectors represent shifts in species composition over time.

all plots is provided in Table SI2.

5. Discussion

We contribute to growing evidence that ice-wedge degradation is widespread throughout the Arctic by showing that most degradation in northeast Alaska occurred since 1950 and accelerated with more frequent extremely warm and wet summers since 1989 (Jones et al., 2013; Jorgenson et al., 2015a; Frost et al., 2018). The degradation was predominantly associated with older surficial deposits of mid-early Holocene or late Pleistocene age with large ice wedges and we believe the rapid degradation is representative of older terrain in northern Alaska. We caution extrapolating trends to younger floodplain and drained-lake basins, which predominantly have low-centered polygons with narrower ice wedges. The combined areal extent of undegraded and degraded ice wedges covered 29% of the study area in 1950, and the extent of all degraded stages combined increased from 2% to 19% within an area of concentrated thermokarst. Thus, 66% of the wedges had partially degraded by 2018. When tracking stages, degradation-initial (DI) peaked at 9% of the area in 2000, degradation-advanced (DA) peaked at 4.5% during 2006–2014, and stabilization-initial (SI) was still trending upward at 12% in 2018, indicating the affected area was transitioning from degradation to stabilization. The mean age of DA in 2018 was 40 yrs., indicating the much of the degradation already was many decades old. We attribute the slowdown in initial degradation during the last two decades to two factors. First, the amount of undegraded ice wedges has been reduced to one-third, indicating the area has already past peak degradation, Second, drainage integration likely plays an important role in removing impounded water from the surface, thereby reducing the positive feedback that surface water plays in soil warming and permafrost degradation (Jorgenson et al., 2010b).

Ice-wedge degradation is radically transforming the hydrology, soils, and vegetation of tussock tundra ecosystems over a decadal time-scale. Surface collapse from the partially degrading ice wedges results in a mosaic of high-centered polygons and deep troughs with impounded water, providing positive feedback that increases ground temperatures (Jorgenson et al., 2015a; Ward Jones et al., 2020). Impounded water causes a complete shift in species composition from tussock tundra with deciduous and evergreen shrubs to an aquatic moss and forb community in DA. Due to soil slumping along the margins of the steep troughs and rapid colonization of aquatic mosses, the pits begin to stabilize with a decrease in active-layer thickness. In SI aquatic sedges grow inward from the trough margins into the thickening (often floating) moss mat and in stabilization-advanced (SA) the diversity of wet-adapted forbs, sedges, and mosses increases. In a newly described stabilization-very advanced (SAV) stage, which develops over centuries, deciduous shrubs return to being dominant, although species diversity remains low. We expect that it would take millennia for composition to recover to that of tussock tundra, because tussock tundra is a very late-successional ecosystem and individual tussocks typically are hundreds of years old. Soils are also transformed in terms of the peat materials and cryostructures in the frozen soil, reflecting the thermal adjustments that accompany the changes in peat and surface water. The formation of a new ice-rich intermediate layer begins in the late DA stage and by SA the aggradation of segregated ice heaves the surface above water level, thus reducing surface temperatures. By SAV, the surface returns almost to the level of the polygon centers. Together the added soil materials, development of a new intermediate layer, and surface heaving that favors surface drying, create a new quasi-stable state that reduces the vulnerability of the deeper wedge ice to future warming. The stabilization process, however, is too slow to have affected the current slow-down in rates of ice-wedge degradation (discussed above). The transitions we observed at Jago were similar to those for tussock tundra at Fish Creek (Jorgenson et al., 2006), while changes in species composition at Prudhoe Bay (Jorgenson et al., 2015a) were somewhat different because of the alkaline soils. Previous studies of vegetation/soil relationships in patterned ground, however, have focused mainly on polygon center to trough differences or polygon evolution (Billings and Peterson, 1980; Minke et al., 2009; Wolter et al., 2016) and not succession in the troughs.

Our results reinforce the concept that ice wedges go through a sequence of degradation and stabilization stages over a period of decades, yet we are finding that the transitions are more complicated (Kanevskiy et al., 2017), with frequent alternative trajectories as degradation of earlier stages is halted and later stages undergo renewed degradation. Particularly problematic is the transition from DA to SI. Repeated coring indicates reticulate and ataxitic cryostructures can develop in thermokarst pits, revealing the initial onset of stabilization can occur under deeper water. In this study we differentiated this stage as degradation-advanced-halted (DAH) as a subset of the DA class because it cannot be differentiated through remote sensing, and we are uncertain about whether newly aggraded segregated ice above the wedge ice is permanent. Furthermore, cryostructures in 2018 indicated vertical stabilization even while DA pits along the transect continued to expand laterally from 2009 to 2018. Therefore, we have maintained SI

Table 1
Mean (n = 3) percent cover of plant species (gradient-oriented list) by degradation stage and year within the monitoring plots. Stages are PC = polygon centers, UD = undegraded, DI = degradation initial, SA = stabilization advanced, SI = stabilization initial, DA = degradation advanced. Bold values indicate large, directional increase.

		PC			UD	DI			SA			SI			DA		
Species	GF	09	11	16	18	09	11	16	09	11	16	09	11	16	09	11	16
Cassiope tetragona	*E*	5	7	3	0												
Rhodo dendron tomen tosum. decum.	*E*	3	2	1				0									
Cladonia sp.	*L*	1	1	1													
Crustose lichen	*L*	1	0	0													
Vaccinium uliginosum	*D*	1	0	2													
Flavocetraria cucullata	*L*	1	0	0													
Thamnolia vermicularis	*L*	2	1	1													
Cetraria islandica	*L*		1														
Stereocaulon alpinum	*L*		0	1													
Tephroseris atropurpurea	*F*		1	1	1												
Saussurea angustifolia	*F*	2	1	1	0												
Bistorta plumosa	*F*	2	2	1	3												
Salix phlebophylla	*D*	1	1	1			2										
Dicranum sp.	*M*	5	5	3	2		1										
Ptilidium ciliare	*M*	5	3	3	5			2									
Vaccinium vitis-idaea	*E*	15	10	7	5		0	3									
Aulacomnium turgidum	*M*	5	8	4			5	0					1				
Arctagrostis latifolia	*G*	1	0	0		2	4	3		0							
Bistorta vivipara	*F*		2	0			1	0									
Peltigera aphthosa	*L*	1	2	5	4		1	2									
Pyrola grandiflora	*F*	2	1	2	1		1	2									
Betula nana	*D*	10	9	6	2	4	2	6									
Dryas integrifolia	*E*	6	12	8	5	5	3	5									
Hylocomium splendens	*M*	25	30	26	26	6	10	11									
Tomentypnum nitens	*M*	9	12	7	25	13	11	8									
Carex bigelowii	*S*	3	9	11	19	10	10	15									
Eriophorum vaginatum	*T*	18	12	28	14	4	5	4		0				0			
Salix pulchra	*D*	13	11	16	11	10	12	11	1	0					1		
Salix reticulata	*D*	3	1	2	6	3	2	3									
Aulacomnium palustre	*M*	8	6	6	13	8	10	3	1	2	2						
Poa arctica	*G*	1	1	1		2	1	0	1								
Sphagnum warnstorfii	*M*	2	0	1				0					4	1			
Valeriana capitata	*F*		0	0	1	1	2	2									
Petasites frigidus	*F*		1	1	4	1	2	1									
Sanionia uncinata	*M*		1	1	5		2										
Polytrichum strictum	*M*		1	2	0		0	1									
Stellaria sp.	*F*		0	1	0		0	0									
Arctous rubra	*D*			2				2									
Nephroma expallidum	*L*			2				1									
Orthilia secunda	*F*		1		1		1	1									
Pedicularis capitata	*F*		0	1	2		0										
Sphagnum sp.	*M*			0	1												
Salix rotundifolia	*D*					3											
Polemonium acutiflorum	*F*						0	1									
Saxifraga hirculus	*F*						0	0									
Cardamine polemonioides	*F*				1		2	1		0							
Eriophorum angustifolium	*S*	1	1	8	5	**20**	**26**	**40**	2	2	3	1	4	3	**1**	**1**	**11**
Caltha palustris	*F*					1	1	0	1	0	0		0	0			
Saxifraga cernua	*F*					1	1	0	1	0	1						
Bryum pseudotriquetrum	*M*						5		1	2							
Mnium sp.	*M*							4		2	1						
Carex chordorrhiza	*S*								5	6	4						
Epilobium palustre	*F*								0	0	0						
Festuca rubra	*G*								1	1							
Sarmentypnum sarmentosum	*M*								3	0							
Campylium stellatum	*M*					8	7	1			1		3	1			
Comarum palustre	*F*					4	3	4	10	6	5		1	0		0	1
Meesia triquetra	*M*				1	3	2	3	6	7	12	5	6	8			
Carex aquatilis	*S*					**8**	**13**	**17**	27	20	29	**27**	**28**	**40**		**2**	**12**
Calliergon giganteum	*AM*				4	1	1	6	38	36	21	18	24	6			**7**
Hamatocaulis lapponicus	*AM*						1	2	35	43	35	**20**	**17**	**27**	**30**	**35**	**62**
Eriophorum russeolum c.f.	*S*							1	**6**	**12**	**20**	3	3	9			
Sparganium hyperboreum	*F*														**6**	**31**	**24**
Bare Soil				1	0		1										5
Water		8	22	7	4	13	27	13	15	34	20	4	31			1	

Growthforms: evergreen shrub (E), deciduous shr. (D), forb (F), grass (G), sedge (S), tusssock (T), moss(M), aquatic moss(AM), lichen(L).

as a more distinctive stage characterized by development of aquatic sedges and newly formed sedge and fen-moss peat.

The factors leading to initial stabilization remain uncertain. The accumulation of soil above the ice wedges from slumping of the steep sidewalls of the troughs likely is an important factor (Fig. SI16), as evidenced by increased soil thickness in DAH. Yet oddly, accumulation of protective soil was not evident in the more widely sampled SI stage (Fig. 9). This thicker soil accumulation in DAH, along with the unusually wide troughs, suggests that lateral thawing has expanded beyond the ice wedges into ice-rich soils in the adjacent polygons, and may be a more recent phenomenon associated with more frequent extremely warm-wet summers. More data also are needed on the thermal effects of the rapid accumulation of aquatic mosses, which can reduce convective heating transfer at the bottom of the ponds, and on the effects of thick ice formed in the winter in the pits, which adds a large latent heat content and delays summer thawing of underlying soils. Finally, we need to understand the role of nutrients released during degradation in stimulating plant growth, which we hypothesize is a powerful negative feedback that facilitates stabilization.

Remote sensing of ice-wedge degradation using high-resolution imagery has been improving rapidly, but challenges remain (Jorgenson and Grosse, 2016). Manual interpretation (Jorgenson et al., 2015a; Steedman et al., 2016) and spectral classification (Jorgenson et al., 2006; Necsoiu et al., 2013; Frost et al., 2018) have been used to map thermokarst troughs and pits in small areas. Elevation differencing of repeat DEMs has been effective at quantifying ice-wedge degradation (Jones et al., 2013; Jones et al., 2015), and high-resolution imagery acquired by unmanned aerial systems have been used to characterize polygonal terrain (Lousada et al., 2018). Recently, automated techniques have been developed to map polygonal landforms using high-resolution optical imagery and/or DEMs (Abolt et al., 2019; Zhang et al., 2020; Frappier and Lacelle, 2021; Rettelbach et al., 2021; Witharana et al., 2021). Differentiating degradation stages across a time-series of imagery, as was done through manual interpretation in this study, remains a challenge for automated techniques. An even bigger challenge is the difficulty in estimating ice-wedge distribution and volume (Ulrich et al., 2014; Bernard-Grand'Maison and Pollard, 2018). Often polygonal patterns indicating underlying ice wedges are not evident, particularly on slopes, and we have often encountered ice wedges in high polygon centers, so mapping of polygonal patterns underestimates ice-wedge volume, particularly in older landscapes. Furthermore, volume estimates typically involve assumptions of ice-wedge dimensions, which can be highly variable and poorly quantified.

Ice-wedge degradation has large implications for arctic land cover change, hydrology, tundra productivity, lake expansion and drainage, soil carbon balance, trace gas emissions, and wildlife (caribou, passerines, shorebirds). Regional analyses of landscape change in northern Alaska (Jorgenson et al., 2015b; Jorgenson et al., 2018) have attributed measurable vegetation shifts to recent thermokarst and wetting, predominantly from ice-wedge degradation. We suspect the recent shift from tundra "greening" to "browning", as measured by satellite NDVI (Phoenix and Bjerke, 2016; Heijmans et al., 2022), may partially be related to robust plant growth during the DI stage, and the recent "browning" effect in tundra ecosystems due to waterbody expansion during the DA stage.

Expansion of the drainage network and reorganization of channel connections caused by ice-wedge degradation, ultimately affect surface-water storage, runoff and export of dissolved organic carbon from tundra. This hydrologic reorganization also affects snow meltwater and summer subsurface flow from polygon centers to troughs (Koch et al., 2018) leading to drying of polygon centers (Perreault et al., 2017). Ice-wedge degradation also is a major contributor to thermokarst lake development, either in Holocene-age landscapes with very high ice-wedge volume or in extremely ice-rich silty deposits of late Pleistocene age with large syngenetic ice wedges (Grosse et al., 2013; Jones et al., 2022). After lake formation, catastrophic drainage of lakes through thawing ice wedges is a major contributor to lake drainage (Jones et al., 2020).

Effects on soil carbon loss or accumulation remains poorly understood. While our data suggest that surface peat materials increase measurably through the sequence, the data are highly variable and the effects of changing peat materials with variable carbon densities remain unknown. Methane emissions increase substantially in thermokarst troughs (Negandhi et al., 2013; Wainwright et al., 2015; Wickland et al., 2020), but varying rates across the stages, along with the changes in abundance of each stage over time, complicate the analysis of the net effects on methane emissions (Wickland et al., 2020).

Finally, a large concern from our results is the effect of changing vegetation on wildlife, particularly passerines, shorebirds, and caribou, with both winners and losers (Marcot et al., 2015). Tussock tundra and moist sedge-shrub tundra are ranked as the most highly used tundra habitats of many birds, including willow ptarmigan, American golden-plover, Baird's sandpiper, buff-breasted sandpiper, savannah sparrow, and Lapland longspur (Martin et al., 2009). Habitat heterogeneity of thermokarst terrain, however, has been linked to higher nest densities of some species, such as American golden plover, semipalmated sandpipers, and red-necked phalarope (Troy, 2000). Effects on caribou are of particular concern because tussock (*Eriophorum vaginatum*) flowers emerge at snowmelt and are a highly nutritious forage species during the short calving season (Jorgenson et al., 2002). In our study area, tussock tundra and moist-sedge shrub tundra, which often has tussocks at low density, lost 8.5% absolute area (19.5% relative loss) combined from 1988 to 2018. This represents a large loss of critical habitat within the core calving area of the Porcupine Caribou Herd, and the caribou are an essential subsistence resource for native villages within the herd's range.

6. Conclusion

We found ice-wedge thermokarst was widespread and rapidly transforming the hydrology, soils, and vegetation of tundra ecosystems through a sequence of degradation and stabilization stages. Advanced degradation was widespread on older terrain, and degradation (all stages combined) increased from 2% in 1950 to 19% area in 2018. This facilitated integration and reorganization of the drainage network as thermokarst troughs expanded and connected. Degradation created large changes in microtopography, trough widths, water depths, depth to wedge ice, pH, soil and ground ice characteristics, and thermal regimes among five principal stages. In response to environmental changes, plant community composition completely shifted from dominance of deciduous and evergreen shrubs in tussock tundra in the undegraded stage to dominance of aquatic mosses and forbs in flooded depressions in degradation-advanced stage. Soil slumping and aquatic moss growth halted the degradation in shallow ponds, and in the stabilization-advanced stage with re-aggrading ground ice and surface heaving the diversity of wet-adapted forbs, sedges, and mosses increased. Recovery back to tussock tundra, however, is likely to take millennia. This decadal-scale transformation will eventually affect 10–30% of the arctic land surface that corresponds to the subsurface coverage of vulnerable ice wedges, and has major implications for arctic land cover, tundra productivity, lake expansion and drainage, altering soil formation and soil-carbon balance, trace-gas emissions, and caribou and bird populations.

Data availability statement

Data are available at the NSF Arctic Data Center, https://arcticdata.io/catalog/data. Soil and cryostructure data by Jorgenson and Kanevskiy (2015, 2020) (doi:10.18739/A28K8J; doi:10.18739/A22J6853K). Vegetation, Soils, and Site-Environmental Data 2009-2018 by Jorgenson and Kanevskiy (2022).

Declaration of Competing Interest

The authors declare that they have no known competing financial interests or personal relationships that could have appeared to influence the work reported in this paper.

Data availability

Data are available at the NSF Arctic Data Center, https://arcticdata.io/catalog/data. Soil and cryostructure data by Jorgenson and Kanevskiy (2015, 2020)(doi:10.18739/A28K8J; doi:10.18739/A22J6853K). Vegetation, Soils, and Site-Environmental Data 2009-2018 by Jorgenson and Kanevskiy (2022).

Acknowledgements

Research was fund by NSF (ARC1023623 and OPP1820883 to PI Shur, PTE1722572 to PI Liljedahl, and OIA1929170 to PI Jones). US Fish and Wildlife Service and Alaska Dep. Geological and Geophysical Surveys provided additional personnel and logistical support. We thank Dave Swanson and an anonymous reviewer for their helpful comments. Use of trade, firm, or product names does not imply endorsement by the U.S. Government. The authors declare no conflict of interests in this research.

Appendix A. Supplementary data

Supplementary data to this article can be found online at https://doi.org/10.1016/j.gloplacha.2022.103921.

References

Abolt, C.J., Young, M.H., Atchley, A.A., Wilson, C.J., 2019. Brief communication: Rapid machine-learning-based extraction and measurement of ice wedge polygons in high-resolution digital elevation models. Cryosphere 13 (1), 237–245. https://doi.org/10.5194/tc-13-237-2019.

AMAP, 2017. Snow, Water, Ice and Permafrost in the Arctic (SWIPA) 2017. Arctic Monitoring and Assessment Programme, Oslo, Norway.

Arendt, A., Walsh, J., Harrison, W., 2009. Changes of Glaciers and climate in Northwestern North America during the late Twentieth Century. J. Clim. 22, 4117–4134. https://doi.org/10.1175/2009JCLI2784.1.

Bernard-Grand'Maison, C., Pollard, W., 2018. An estimate of ice wedge volume for a High Arctic polar desert environment, Fosheim Peninsula, Ellesmere Island. Cryosphere 12 (11), 3589–3604. https://doi.org/10.5194/tc-12-3589-2018.

Billings, W.D., Peterson, K.M., 1980. Vegetational change and ice-wedge polygons through the thaw lake cycle in Arctic Alaska. Arct. Alp. Res. 12 (4), 413–432.

Black, R.F., 1952. Growth of ice-wedge polygons in permafrost near Barrow, Alaska. Geol. Soc. Am. Bull. 63 (12), 1235–1236.

Black, R.F., 1976. Periglacial features indicative of permafrost: ice and soil wedges. Quat. Res. 6, 3–26.

Blok, D., Schaepman-Strub, G., Bartholomeus, H., Heijmans, M., Maximov, T.C., Berendse, F., 2011. The response of Arctic vegetation to the summer climate: relation between shrub cover, NDVI, surface albedo and temperature. Environ. Res. Lett. 6, 035502 https://doi.org/10.1088/1748-9326/6/3/035502.

Bret-Harte, M.S., Mack, M.C., Shaver, G.R., Huebner, D.C., Johnston, M., Mojica, C.A., Pizano, M.C., Reiskind, J.A., 2013. The response of arctic vegetation and soils following the Anaktuvuk River fire of 2007. Philosphical Transactions of the Royal Society B 368 (20120490). https://doi.org/10.1098/rstb.2012.0490.

Brown, J., Grave, N.A., 1979. Physical and thermal disturbance and protection of permafrost [pp]. U.S. Army Cold Regions Res. Eng. Lab. Hanover, NH. Special Rep. 79-5, 1–42.

Brown, J., Ferrians, O.J., Heginbottom Jr., J.A., Melnikov, E.S., 1997. Circum-Arctic map of permafrost and ground ice conditions. U.S. Geological Survey. Reston, Virginia. CP-45.

Burn, C.R., O'Neill, H.B., 2015. Subdivision of Ice-wedge Polygons, Western Arctic Coast. In GEOQuebec 2015. Canadian Geotechnical Society, Quebec, QC.

Carter, L.D., Ferrians, O.J., Galloway, J.P., 1986. Engineering-geologic maps of northern Alaska, coastal plain and foothills of the Arctic National Wildlife Refuge. U.S. Geological Survey. Open File Rep. 86-334 2 (sheets).

Chapin, F.S.I., Peterson, G., Berkes, F., Callaghan, T.V., Angelstam, P., Apps, M., Beier, C., Bergeron, Y., Crepin, A.-S., Danell, K., Elmqvist, T., Folke, C., Forbes, B., Fresco, N., Juday, G., Niemela, J., Shvidenko, A., Whiteman, G., 2004. Resilence and vulnerability of northern regions to social and environmental change. AMBIO J. Human Environ. 33 (6), 344–349. https://doi.org/10.1579/0044-7447-33.6.344.

Chen, Y., Lara, M.J., Jones, B.M., Frost, G.V., Hu, F.S., 2021. Thermokarst acceleration in Arctic tundra driven by climate change and fire disturbance. One Earth 4 (12), 1718–1729. https://doi.org/10.1016/j.oneear.2021.11.011.

Christiansen, H.H., Matsuoka, N., Watanabe, T., 2016. Progress in understanding the dynamics, internal structure and palaeoenvironmental potential of ice wedges and sand wedges. Permafr. Periglac. Process. 27 (4), 365–376. https://doi.org/10.1002/ppp.1920.

Couture, N.J., Pollard, W.H., 2017. A model for quantifying ground-ice volume, Yukon Coast, Western Arctic Canada. Permafr. Periglac. Process. 28 (3), 534–542. https://doi.org/10.1002/ppp.1952.

Farquharson, L.M., Romanovsky, V.E., Cable, W.L., Walker, D.A., Kokelj, S., Nicolsky, D., 2019. Climate change drives widespread and rapid thermokarst development in very cold permafrost in the Canadian High Arctic. Geophys. Res. Lett. 46 (12), 6681–6689. https://doi.org/10.1029/2019GL082187.

Fortier, D., Allard, M., Shur, Y., 2007. Observation of rapid drainage system development by thermal erosion of ice wedges on Bylot Island, Canadian Arctic Archipelago. Permafr. Periglac. Process. 18 (3), 229–243. https://doi.org/10.1002/ppp.595.

Frappier, R., Lacelle, D., 2021. Distribution, morphometry, and ice content of ice-wedge polygons in Tombstone Territorial Park, Central Yukon, Canada. Permafr. Periglac. Process. 32 (4), 587–600. https://doi.org/10.1002/ppp.2123.

Fraser, R., Kokelj, S., Lantz, T., McFarlane-Winchester, M., Olthof, I., Lacelle, D., 2018. Climate sensitivity of high Arctic permafrost terrain demonstrated by widespread ice-wedge thermokarst on Banks Island. Remote Sens. 10 (6), 954. https://doi.org/10.3390/rs10060954.

French, H.M., Shur, Y., 2010. The principles of cryostratigraphy. Earth Sci. Rev. 101, 190–206. https://doi.org/10.1016/j.earscirev.2010.04.002.

Frost, G.V., Christopherson, T., Jorgenson, M.T., Liljedahl, A.K., Macander, M.J., Walker, D.A., Wells, A.F., 2018. Regional patterns and asynchronous onset of ice-wedge degradation sihce the mid-2oth Century in Arctic Alaska. Remote Sens. 10, 3390. https://doi.org/10.3390/rs10081312.

Grosse, G., Jones, B., Arp, C., 2013. Thermokarst lakes, drainage, and drained Basins. In: John, J.F., Shroder, F. (Eds.), Treatise on Geomorphology, vol. 8. Academic Press, pp. 325–353. https://doi.org/10.1016/B978-0-12-374739-6.00216-5.

Grosse, G., Goetz, S., McGuire, A.D., Romanovsky, V.E., Schuur, E.A., 2016. Changing permafrost in a warming world and feedbacks to the Earth system. Environ. Res. Lett. 11 (4), 040201. https://iopscience.iop.org/article/10.1088/1748-9326/11/4/040201/meta.

Harry, D.G., Gozdzik, J.S., 1988. Ice wedges: growth, thaw transformation, and palaeoenvironmental significance. J. Quat. Sci. 3, 39–55. https://doi.org/10.1002/jqs.3390030107.

Heijmans, M.M., Magnússon, R.Í., Lara, M.J., Frost, G.V., Myers-Smith, I.H., van Huissteden, J., Jorgenson, M.T., Fedorov, A.N., Epstein, H.E., Lawrence, D.M., Limpens, J., 2022. Tundra vegetation change and impacts on permafrost. Nat. Rev. Earth Envir. 3 (1), 68–84. https://doi.org/10.1038/s43017-021-00233-0.

Heim, R.J., Bucharova, A., Brodt, L., Kamp, J., Rieker, D., Soromotin, A.V., Yurtaev, A., Hölzel, N., 2021. Post-fire vegetation succession in the Siberian subarctic tundra over 45 years. Sci. Total Environ. 760, 143425 https://doi.org/10.1016/j.scitotenv.2020.143425.

Helbig, M., Boike, J., Langer, M., Schreiber, P., Runkle, B.R., Kutzbach, L., 2013. Spatial and seasonal variability of polygonal tundra water balance: Lena River Delta, northern Siberia (Russia). Hydrogeol. J. 21 (1), 133–147. https://doi.org/10.1007/s10040-012-0933-4.

Hu, F.S., Higuera, P.E., Duffy, P., Chipman, M.L., Rocha, A.V., Young, A.M., Kelly, R., Dietze, M.C., 2015. Arctic tundra fires: natural variability and responses to climate change. Front. Ecol. Environ. 13 (7), 369–377. https://doi.org/10.1890/150063.

Irrgang, A.M., Bendixen, M., Farquharson, L.M., Baranskaya, A.V., Erikson, L.H., Gibbs, A.E., Ogorodov, S.A., Overduin, P.P., Lantuit, H., Grigoriev, M.N., Jones, B.M., 2022. Drivers, dynamics and impacts of changing Arctic coasts. Nat. Rev. Earth Envir. 3 (1), 39–54. https://doi.org/10.1038/s43017-021-00232-1.

Joly, K., Jandt, R.R., Klein, D.R., 2009. Decrease of lichens in Arctic ecosystems: the role of wildfire, caribou, reindeer, competition and climate in North-Western Alaska. Polar Res. 28, 433–442. https://doi.org/10.3402/polar.v28i3.6134.

Jones, B.M., Stoker, J.M., Gibbs, A.E., Grosse, G., Romanovsky, V.E., Douglas, T.A., Kinsman, N.E.M., Richmond, B.M., 2013. Quantifying landscape change in an arctic coastal lowland using repeat airborne LiDAR. Environ. Res. Lett. 8, 045025 https://doi.org/10.1088/1748-9326/8/4/045025.

Jones, B.M., Grosse, G., Arp, C.D., Liu, L., Miller, E.A., Hayes, D.J., Larsen, C., 2015. Recent arctic tundra fire initiates widespread thermokarst development. Sci. Rep. 5, 15865. https://doi.org/10.1038/srep15865.

Jones, B.M., Arp, C.D., Grosse, G., Nitze, I., Lara, M.J., Whitman, M.S., Farquharson, L.M., Kanevskiy, M., Parsekian, A.D., Breen, A.L., Ohara, N., 2020. Identifying historical and future potential lake drainage events on the western Arctic coastal plain of Alaska. Permafr. Periglac. Process. 31 (1), 110–127. https://doi.org/10.1002/ppp.2038.

Jones, B.M., Grosse, G., Farquharson, L.M., Roy-Léveillée, P., Veremeeva, A., Kanevskiy, M.Z., Gaglioti, B.V., Breen, A.L., Parsekian, A.D., Ulrich, M., Hinkel, K.M., 2022. Lake and drained lake basin systems in lowland permafrost regions. Nat. Rev. Earth Envir. 3 (1), 85–98. https://doi.org/10.1038/s43017-021-00238-9.

Jorgenson, M.T., Grosse, G., 2016. Remote sensing of landscape change in permafrost regions. Permafr. Periglac. Process. 27 (4), 324–338. https://doi.org/10.1002/ppp.1914.

Jorgenson, M.T., Shur, Y., Walker, H.J., 1998. Factors affecting evolution of a permafrost dominated landscape on the Colville River Delta, northern Alaska. In: Lewkowicz, A.G., Allard, M. (Eds.), Proceedings of Seventh International Permafrost Conference. Collection Nordicana, no. 57, pp. 523–530. In: https://www.uspermafrost.org/conference-proceedings.

Jorgenson, J.C., Udevitz, M.S., Felix, N.A., 2002. Section 5: forage quantity and quality. In: Douglas, D.C., Reynolds, P.E., Rhode, E.B. (Eds.), Arctic Refuge Coastal Plain Terrestrial Wildlife Research Summary. U.S. Geological Survey. Biological Science Report USGS/BRD/BSR-2002-0001, pp. 46–50.

Jorgenson, M.T., Shur, Y.L., Pullman, E.R., 2006. Abrupt increase in permafrost degradation in Arctic Alaska. Geophys. Res. Lett. 33, L02503. https://doi.org/10.1029/2005GL024960.

Jorgenson, M.T., Yoshikawa, K., Kanveskiy, M., Shur, Y.L., Romanovsky, V., Marchenko, S., Grosse, G., Brown, J., Jones, B., 2008. Permafrost characteristics of Alaska. In: Kane, D.L., Hinkel, K.M. (Eds.), Proceedings Ninth International Conference on Permafrost. University of Alaska, Fairbanks, AK, pp. 121–122.

Jorgenson, J.C., Ver Hoef, J., Jorgenson, M.T., 2010a. Long-term recovery patterns of arctic tundra after winter seismic exploration. Ecol. Appl. 20 (1), 205–221. https://doi.org/10.1890/08-1856.1.

Jorgenson, M.T., Romanovsky, V., Harden, J., Shur, Y., O'Donnell, J., Schuur, E.A.G., Kanevskiy, M., Marchenko, S., 2010b. Resilience and vulnerability of permafrost to climate change. Can. J. For. Res. 40, 1219–1236. https://doi.org/10.1139/X10-060.

Jorgenson, M.T., Kanevskiy, M.Z., Shur, Y., Wickland, K., Nossov, D.R., Moskalenko, N. G., Koch, J., Striegl, R., 2015a. Role of ground-ice dynamics and ecological feedbacks in recent ice-wedge degradation and stabilization. J. Geophys. Res. Earth Surf. 120, 2280–2297. https://doi.org/10.1002/2015JF003602.

Jorgenson, M.T., Marcot, B.G., Swanson, D.K., Jorgenson, J.C., DeGange, A.R., 2015b. Projected changes in diverse ecosystems from climate warming and biophysical drivers in Northwest Alaska. Clim. Chang. 130, 131–144. https://doi.org/10.1007/s10584-014-1302-1.

Jorgenson, J.C., Jorgenson, M.T., Boldenow, M., Orndahl, K., 2018. Landscape change detected over a half century in the Arctic National Wildlife Refuge using high-resolution aerial imagery. Remote Sens. 10 (8), 1305. https://doi.org/10.3390/rs10081305.

Kanevskiy, M.Z., Shur, Y., Fortier, D., Jorgenson, M.T., Stephani, E., 2011. Cryostratigraphy of late Pleistocene syngenetic permafrost (yedoma) in northern Alaska, Itkillik River exposure. Quat. Res. 75, 584–596. https://doi.org/10.1016/j.yqres.2010.12.003.

Kanevskiy, M., Shur, Y., Jorgenson, M.T., Ping, C.L., Michaelson, G.J., Fortier, D., Stephani, E., Dillon, M., Tumskoy, V.E., 2013. Ground ice in the upper permafrost of the Beaufort Sea coast of Alaska. Cold Reg. Sci. Technol. 85, 56–70. https://doi.org/10.1016/j.coldregions.2012.08.002.

Kanevskiy, M., Shur, Y., Jorgenson, T., Brown, D.R., Moskalenko, N., Brown, J., Walker, D.A., Raynolds, M.K., Buchhorn, M., 2017. Degradation and stabilization of ice wedges: Implications for assessing risk of thermokarst in northern Alaska. Geomorphology 297, 20–42. https://doi.org/10.1016/j.geomorph.2017.09.001.

Koch, J.C., Jorgenson, M.T., Wickland, K.P., Kanevksiy, M., Striegl, R., 2018. Ice wedge degradation and stabilization impacts water budgets and nutrient cycling in Arctic trough ponds. J. Geophys. Res. Biogeosci. 123, 2604–2616. https://doi.org/10.1029/2018JG004528.

Kokelj, S.V., Jorgenson, M.T., 2013. Advances in Thermokarst Research. Permafr. Periglac. Process. 24, 108–119. https://doi.org/10.1002/ppp.1779.

Kreig, R.A., Reger, R.D., 1982. Air-photo analysis and summary of landform soil properties along the route of the Trans-Alaska Pipeline System. In: Alaska Div. of Geological and Geophysical Surveys. Fairbanks, AK. Geologic Report, 66 (149 pp).

Lachenbruch, A.H., 1962. Mechanics of Thermal Contraction cracks and Ice-Wedge Polygons in Permafrost. Geological Society of America (Special Paper 70).

Lantuit, H., Overduin, P.P., Wetterich, S., 2013. Recent progress regarding permafrost coasts. Permafr. Periglac. Process. 24, 120–130. https://doi.org/10.1002/ppp.1777.

Leffingwell, E.D.K., 1915. Ground-ice wedges, the dominant form of ground-ice on the north coast of Alaska. J. Geol. 23, 635–654.

Liljedahl, A.K., Hinzman, L.D., Schulla, J., 2012. Ice-Wedge polygon type controls low-gradient watershed-scale hydrology. In: Hinkel, K.M. (Ed.), Tenth International Conference on Permafrost the Northern Publisher, vol. 1, pp. 231–236. In: https://www.uspermafrost.org/conference-proceedings.

Liljedahl, A.K., Boike, J., Daanen, R.P., Fedorov, A.N., Frost, G.V., Grosse, G., Hinzman, L.D., Iijma, Y., Jorgenson, J.C., Matveyeva, N., Necsoiu, M., Raynolds, M., Romanovsky, V.E., Schulla, J., Tape, K.D., Walker, D.A., Wilson, C.J., Yabuki, H., Zona, D., 2016. Pan-Arctic ice-wedge degradation in warming permafrost and its influence on tundra hydrology. Nat. Geosci. 9, 312–318. https://doi.org/10.1038/ngeo2674.

Liljedahl, A.K., Timling, I., Frost, G.V., Daanen, R., 2020. Arctic riparian shrub expansion indicates a shift from streams gaining water to those that lose flow. Comm. Earth Envir. 1 (1), 1–9. https://doi.org/10.1038/s43247-020-00050-1.

Loranty, M.M., Goetz, S.J., 2012. Shrub expansion and climate feedbacks in Arctic tundra. Environ. Res. Lett. 7 (011005) https://doi.org/10.1088/1748-9326/7/1/011005.

Lousada, M., Pina, P., Vieira, G., Bandeira, L., Mora, C., 2018. Evaluation of the use of very high resolution aerial imagery for accurate ice-wedge polygon mapping (Adventdalen, Svalbard). Sci. Total Environ. 615, 1574–1583. https://doi.org/10.1016/j.scitotenv.2017.09.153.

Mackay, J.R., 1972. The world of underground ice. Ann. Assoc. Am. Geogr. 62, 1–22. https://doi.org/10.1111/j.1467-8306.1972.tb00839.x.

Marcot, B.G., Jorgenson, M.T., Lawler, J.P., Handel, C.M., DeGange, A.R., 2015. Projected changes in wildlife habitats in Arctic natural areas of Northwest Alaska. Clim. Chang. 130, 145–154. https://doi.org/10.1007/s10584-015-1354-x.

Martin, P.D., Jenkins, J.L., Adams, F.J., Jorgenson, M.T., Matz, A.C., Payer, D.C., Reynolds, P.E., Tidwell, A.C., Zelenak, J.R., 2009. Wildlife Responses to Environmental Arctic Change. U.S. Fish and Wildlife Service, Fairbanks, AK.

McCune, B., Grace, J.B., 2002. Analysis of Ecological Communities. MjM Software Design, Glendon Beach, OR.

Minke, M., Donner, N., Karpov, N., de Klerk, P., Joosten, H., 2009. Patterns in vegetation composition, surface height and thaw depth in polygon mires in the Yakutian Arctic (NE Siberia): a microtopographical characterisation of the active layer. Permafr. Periglac. Process. 20, 357–368. https://doi.org/10.1002/ppp.663.

Moore, R.D., Fleming, S.W., Menounos, B., Wheate, R., Fountain, A., Stahl, K., Holm, K., Jakob, M., 2009. Glacier change in western North America: influences on hydrology, geomorphic hazards and water quality. Hydrocarb. Process. 23, 42–61. https://doi.org/10.1002/hyp.7162.

Myers-Smith, I.H., Forbes, B.C., Wilmking, M., Hallinger, M., Lantz, T.C., Blok, D., Tape, K.D., Macias-Fauria, M., Sass-Klaassen, U., Lévesque, E., Boudreau, S., 2011. Shrub expansion in tundra ecosystems: Dynamics, impacts and research priorities. Environ. Res. Lett. 6 (045509) https://doi.org/10.1088/1748-9326/6/4/045509.

Necsoiu, M., Dinwiddie, C.L., Walter, G.R., Larsen, A., Stothoff, S.A., 2013. Multi-temporal image analysis of historical aerial photographs and recent satellite imagery reveals evolution of water body surface area and polygonal terrain morphology in Kobuk Valley National Park, Alaska. Environ. Res. Lett. 8 (025007), 1–16. https://doi.org/10.1088/1748-9326/8/2/025007.

Negandhi, K., Laurion, I., Whiticar, M.J., Galand, P.E., Xu, X., Lovejoy, C., 2013. Small thaw ponds: an unaccounted source of methane in the Canadian High Arctic. PLoS One 8 (11), e78204. https://doi.org/10.1371/journal.pone.0078204.

Niittynen, P., Heikkinen, R.K., Luoto, M., 2020. Decreasing snow cover alters functional composition and diversity of Arctic tundra. Proc. Natl. Acad. Sci. 117 (35), 21480–21487. https://doi.org/10.1073/pnas.2001254117.

Nitze, I., Grosse, G., Jones, B.M., Arp, C.D., Ulrich, M., Fedorov, A., Veremeeva, A., 2017. Landsat-based trend analysis of lake dynamics across northern permafrost regions. Remote Sens. 9 (7), 640. https://doi.org/10.3390/rs9070640.

Nitze, I., Grosse, G., Jones, B.M., Romanovsky, V.E., Boike, J., 2018. Remote sensing quantifies widespread abundance of permafrost region disturbances across the Arctic and Subarctic. Nat. Commun. 9 (1), 5423. https://doi.org/10.1038/s41467-018-07663-3.

Osterkamp, T.E., Jorgenson, J.C., 2006. Warming of permafrost in the Arctic National Wildlife Refuge, Alaska. Permafr. Periglac. Process. 17, 65–69.

Perreault, N., Lévesque, E., Fortier, D., Gratton, D., Lamarque, L.J., 2017. Remote sensing evaluation of High Arctic wetland depletion following permafrost disturbance by thermo-erosion gullying processes. Arctic Science 3 (2), 237–253. https://doi.org/10.1139/as-2016-0047.

Phoenix, G.K., Bjerke, J.W., 2016. Arctic browning: extreme events and trends reversing arctic greening. Glob. Chang. Biol. 22 (9), 2960–2962. https://doi.org/10.1111/gcb.13261.

Pollard, W.H., French, H.M., 1980. A first approximation of the volume of ground ice, Richards Island, Pleistocene Mackenzie Delta, Northwest Territories, Canada. Can. J. Earth Sci. 17, 509–516. https://doi.org/10.1139/t80-059.

Raynolds, M.K., Walker, D.A., Verbyla, D., Munger, C.A., 2013. Patterns of change within a tundra landscape: 22-year Landsat NDVI trends in an area of the northern foothills of the Brooks Range, Alaska. Arct. Antarct. Alp. Res. 45 (2), 249–260. https://doi.org/10.1657/1938-4246-45.2.249.

Raynolds, M.K., Walker, D.A., Ambrosius, K.J., Brown, J., Everett, K.R., Kanevskiy, M., Kofinas, G.P., Romanovsky, V.E., Shur, Y., Webber, P.J., 2014. Cumulative geoecological effects of 62 years of infrastructure and climate change in ice-rich permafrost landscapes, Prudhoe Bay Oilfield, Alaska. Glob. Chang. Biol. 20 (4), 1211–1224. https://doi.org/10.1111/gcb.12500.

Raynolds, M.K., Walker, D.A., Balser, A., Bay, C., Campbell, M., Cherosov, M.M., Daniëls, F.J., Eidesen, P.B., Ermokhina, K.A., Frost, G.V., Jedrzejek, B., Jorgenson, M.T., Kennedy, B.E., Kholod, S.S., et al., 2019. A raster version of the Circumpolar Arctic Vegetation Map (CAVM). Remote Sens. Environ. 232 (111297) https://doi.org/10.1016/j.rse.2019.111297.

Rettelbach, T., Langer, M., Nitze, I., Jones, B., Helm, V., Freytag, J.C., Grosse, G., 2021. A quantitative graph-based approach to monitoring ice-wedge trough dynamics in polygonal permafrost landscapes. Remote Sens. 13 (16), 3098. https://doi.org/10.3390/rs13163098.

Romanovskii, N.N., 1985. Distribution of recently active ice and soil wedges in the USSR. In: Church, M., S. O. (Eds.), Field and Theory: Lectures in Geocryology. University of British Columbia, pp. 154–165.

Schuur, E.A., Mack, M.C., 2018. Ecological response to permafrost thaw and consequences for local and global ecosystem services. Annu. Rev. Ecol. Evol. Syst. 49, 279–301. https://doi.org/10.1146/annurev-ecolsys-121415-032349.

Shur, Y., Hinkel, K.M., Nelson, F.E., 2005. The transient layer: implications for geocryology and climate-change science. Permafr. Periglac. Process. 16 (1), 5–17. https://doi.org/10.1002/ppp.518.

Steedman, A.E., Lantz, T.C., Kokelj, S.V., 2016. Spatio-temporal variation in high-Centre polygons and ice-wedge melt ponds, Tuktoyaktuk Coastlands, Northwest Territories. Permafr. Periglac. Process. 28 (1), 66–78. https://doi.org/10.1002/ppp.1880.

Sturm, M., Schimel, J., Michaelson, G.J., Welker, J.M., Oberbauer, S.F., Liston, G.E., Fahnestock, J., Romanovsky, V., 2005. Winter biological processes could help convert Arctic tundra to shrubland. BioScience 55, 17–26. https://doi.org/10.1641/0006-3568(2005)055[0017:WBPCHC]2.0.CO;2.

Troy, D.M., 2000. Shorebirds. In: Truett, J.C., Johnson, S.R. (Eds.), The Natural History of an Arctic Oilfield. Academic Press, pp. 277–303.

Ulrich, M., Grosse, G., Strauss, J., Schirrmeister, L., 2014. Quantifying Wedge-Ice Volumes in Yedoma and Thermokarst Basin Deposits. Permafr. Periglac. Process. 25 (3), 151–161. https://doi.org/10.1002/ppp.1810.

Wainwright, H.M., Dafflon, B., Smith, L.J., Hahn, M.S., Curtis, J.B., Wu, Y., Ulrich, C., Peterson, J.E., Torn, M.S., Hubbard, S.S., 2015. Identifying multiscale zonation and assessing the relative importance of polygon geomorphology on carbon fluxes in an Arctic tundra ecosystem. J. Geophys. Res. Biogeosci. 120 (4), 788–808. https://doi.org/10.1002/2014JG002799.

Walker, H.J., Arnborg, L., 1963. Permafrost and ice-wedge effect on riverbank erosion. In Proceedings, Permafrost, International Conference. National Academy of Sciences. Nat. Res. Council Pub. 1287, 164–171. In: https://www.uspermafrost.org/conference-proceedings.

Walker, D.A., Raynolds, M., Kanevksiy, M., Shur, Y., Romanovsky, V.E., Jones, B., Jorgenson, T., Buchhorn, M., Šibík, J., Breen, A., Kade, A., Watson-Cook, E., Bergstedt, H., Liljedahl, A., Daanen, R., Connor, B., Nicolsky, D., Peirce, J., 2022. Cumulative impacts of a gravel road and climate change in an ice-wedge polygon landscape, Prudhoe Bay, AK. Arctic. Science 8 (1). https://doi.org/10.1139/AS-2021-0014.

Ward Jones, M.K., Pollard, W.H., Amyot, F., 2020. Impacts of degrading ice-wedges on ground temperatures in a high Arctic polar desert system. J. Geophys. Res. Earth Surf. https://doi.org/10.1029/2019JF005173 e2019JF005173.

Wells, A.F., Frost, Gerald V., Macander, M.J., Jorgenson, M.T., Roth, J.E., Davis, W.A., Pullman, E.R., 2020. Integrated terrain unit mapping on the Beaufort Coastal Plain, North Slope, Alaska, USA. Landsc. Ecol. 1-31 https://doi.org/10.1007/s10980-020-01154-x.

Wickland, K.P., Jorgenson, M.T., Koch, J.C., Kanevskiy, M., Striegl, R.G., 2020. Carbon dioxide and methane flux in a dynamic arctic tundra landscape: Decadal-scale impacts of ice wedge degradation and stabilization. Geophys. Res. Lett. 47 (22) https://doi.org/10.1029/2020GL089894 e2020GL089894.

Witharana, C., Bhuiyan, M.A.E., Liljedahl, A.K., Kanevskiy, M., Jorgenson, T., Jones, B. M., Daanen, R., Epstein, H.E., Griffin, C.G., Kent, K., Ward Jones, M.K., 2021. An object-based approach for mapping tundra ice-wedge polygon troughs from very high spatial resolution optical satellite imager. Remote Sens. 13 (4), 558. https://doi.org/10.3390/rs13040558.

Wolter, J., Lantuit, H., Fritz, M., Macias-Fauria, M., Myers-Smith, I., Herzschuh, U., 2016. Vegetation composition and shrub extent on the Yukon coast, Canada, are strongly linked to ice-wedge polygon degradation. Polar Res. 35 (1), 27489. https://doi.org/10.3402/polar.v35.27489.

Zhang, W., Liljedahl, A.K., Kanevskiy, M., Epstein, H.E., Jones, B.M., Jorgenson, M.T., Kent, K., 2020. Transferability of deep learning Mask R-CNN model for automated mapping of ice-wedge polygons in high-resolution satellite and UAV images. Remote Sens. 12 (1085), 1–20. https://doi.org/10.3390/rs12071085.